International Journal of Mechanical Sciences 274 (2024) 109222



Contents lists available at ScienceDirect

International Journal of Mechanical Sciences

journal homepage: www.elsevier.com/locate/ijmecsci





Hybrid physics-based and data-driven impact localisation for composite laminates☆

Dong Xiao *, Zahra Sharif-Khodaei, M.H. Aliabadi

Department of Aeronautics, Imperial College London, South Kensington, London, SW7 2AZ, United Kingdom

ARTICLE INFO

Keywords:
Structural health monitoring
Impact localisation
Composite laminates
Dispersion relations
Wave velocity profile
Triangulation method

ABSTRACT

The current challenges facing data-driven impact localisation methods primarily involve accurately localising impacts occurring outside the training impact coverage area, particularly for anisotropic composite structures. This study addresses these challenges by integrating the physical dispersion relations of impact-induced waves into the localisation process, thereby enhancing overall accuracy and reducing reliance on extensive training impact data. The dominant impact-induced flexural waves, derived from first-order shear deformation theory and classical laminate theory, exhibit significant dispersion. The phase velocity of these waves is governed by a dispersion equation dependent on structural stiffness, wave frequency, and direction. Solving this dispersion equation for a given wave frequency and known structural stiffness yields a wave velocity profile (WVP). Unlike conventional data-driven methods, which approximate the WVP with a black box and relate the time difference of arrival to the impact location, this study explicitly formulates and optimises the WVP with respect to structural stiffness and wave frequency based on the training impacts. Leveraging the partial derivatives of the dispersion equation, optimisation is performed using fast gradient-based techniques such as the Newton's method and the trust-region reflective algorithm. The optimised WVP is then employed for impact localisation using the triangulation method. Experimental validation of the proposed hybrid physics-based and data-driven impact localisation method involves conducting drop-mass impact testing on a composite laminate flat panel and a stringer-stiffened panel. The localisation results confirm the efficiency and accuracy of the proposed hybrid method with minimal training impact data, demonstrating its capability to accurately localise impacts even for stiffened panels, including those occurring outside the coverage area of the training impacts.

1. Introduction

Low-velocity impacts, such as those resulting from tool drops, applied to composite laminates can induce Barely Visible Impact Damage (BVID), posing a significant threat to structural integrity [1–5]. To address the detection and characterisation of these damage-causing impacts, passive sensing techniques for structural health monitoring (SHM) have garnered considerable attention and application, particularly within the aerospace sector [6]. Passive sensing systems for SHM involve the deployment of passive sensors affixed to the structure, which remain in a low-power state during normal operation and activate to record and store structural responses only upon detection of an external impact [7,8]. Leveraging the recorded passive sensor signals, a primary focus of passive SHM revolves around accurately localising impacts, reconstructing impact forces, and crucially, assessing the impact damages [9].

The foundational axioms of SHM, as concluded by Farrar [10], highlight the inherent limitation wherein sensors alone cannot directly measure damage; instead, damage assessment necessitates a comparative analysis between two system states. Conversely, the estimation of impact location and impact force history can be achieved solely through analysis of passive sensor signals. These insights drive the exploration of indirect methodologies for impact damage assessment. For instance, the development of a digital twin model [11] that integrates estimated impact location and reconstructed impact force history into a numerical impact model facilitates impact damage assessment. In any circumstance, the effectiveness and precision of impact localisation methods are paramount, as they provide crucial spatial data concerning potential impact damage.

Considerable research efforts have been dedicated to the advancement of impact localisation methods [12], which are typically categorised into model-based, modal-based, transfer function-based and

☆ In this work, a novel hybrid physics-based and data-driven method for impact localisation on composite laminates is developed, which enables the localisation of impacts outside the training impact coverage area and the reduction of training impacts required.

* Corresponding author.
E-mail addresses: d.xiao21@imperial.ac.uk (D. Xiao), z.sharif-khodaei@imperial.ac.uk (Z. Sharif-Khodaei), m.h.aliabadi@imperial.ac.uk (M.H. Aliabadi).

https://doi.org/10.1016/j.ijmecsci.2024.109222
Received 14 December 2023; Received in revised form 6 March 2024; Accepted 24 March 2024
Available online 30 March 2024
0020-7403/© 2024 The Author(s). Published by Elsevier Ltd. This is an open access article under the CC BY-NC-ND license (http://creativecommons.org/licenses/by-nc-nd/4.0/).

wave propagation-based methods. Model-based techniques, rooted in numerical impact simulation models such as the Finite Element Method (FEM), aim to determine impact location either by minimising disparities [13,14] or by maximising correlation coefficients [15] between predicted and measured responses across all potential loading points. For instance, El-Bakari [14] employed the particle swarm optimisation algorithm based on beam theory to minimise the fitness function derived from impulse response function for impact localisation on an elastic beam. In a recent work, Liu [15] constructed a FEM model and developed a hierarchical approach to identify the numbers, locations, and forces of impacts, incorporating partition optimisation and polynomial fitting strategies to expedite impact localisation. However, these models heavily rely on accurate knowledge of material properties [16] and boundary conditions [17], which can be challenging to obtain in real-world applications. Moreover, real-time impact localisation using FEM is often impractical, as identifying a single target impact typically entails conducting hundreds of impact simulations, even when employing surrogate-assisted efficient global optimisation techniques [18].

Modal analysis, as a widely-used technique in structural dynamics [19], can also facilitate impact localisation. This method reveals that the distinct contributions of modal modes in the structural response serve as signatures for the impact location. Goutaudier [20,21] successfully identified both the locations and severities of impacts on a metallic plate using only a single accelerometer, leveraging this modal information. However, it is important to note that obtaining mode shapes from experiments is a prerequisite for this method, which may limit its applicability.

The transfer function between the impact response and impact excitation offers valuable physical information for impact localisation. The time reversal technique [22] aids in this process by correlating transfer functions with impact responses, with the highest time reversal correlations indicating the impact location. These transfer functions can be obtained through experiments conducted prior to impact localisation. For instance, Ciampa [23] utilised a pre-collected transfer function database to identify impacts on composite structures using time reversal with only one passive sensor. Additionally, transfer functions can be approximated using a FEM model. In a recent study by Yu [24], time-domain spectral FEM was employed to simulate the re-emitted wavefield by reversing the impact sensor response for impact localisation. Furthermore, transfer functions can be estimated using a data-driven approach with training impact data related to the sensor signals and impact force. Simone [25] and Chen [26] accurately located impacts on composite and aluminum plates, respectively, using time reversal based on densely-distributed training impact data. However, it is noteworthy that time reversal relies on the linear reciprocity theorem, which may not be entirely applicable when boundary conditions significantly influence structural responses [27].

The wave propagation method, grounded in the physical relationship that the distance travelled by impact-induced waves is the product of wave propagation velocity and propagation time, offers a means to locate impacts. With knowledge of the wave velocity profile (WVP), impacts on composite structures can be estimated in two-dimensional coordinates using triangulation with a minimum of three sensors [28]. This WVP can be determined through numerical simulations or experimental measurements. However, it is crucial to consider the specific type of wave, as the wave propagation velocity and time difference of arrival (TDOA) are wave-dependent. Impact experiments [29–31] demonstrate that impacts simultaneously generate in-plane extensional waves, and out-of-plane flexural waves in the structure. The in-plane extensional wave typically exhibits higher frequency and velocity compared to the flexural wave, although the flexural wave carries the majority of the energy and dominates the impact-induced waves.

Due to the high-frequency and low-amplitude nature of in-plane extensional waves, Capineri [32] and Bulletti [33] typically designed an analog front-end to capture these high-frequency waves for impact localisation. The sampling frequency required to capture extensional waves typically exceeds several hundred thousand hertz. Zhu [34] conducted experimental comparisons between extensional waves and flexural waves for TDOA extraction using the Akaike Information Criterion (AIC). Extensional waves were selected for impact localisation based on the challenges associated with AIC method for TDOA estimation. Conversely, Meo [35] utilised wavelet transform to extract TDOA and WVP from flexural waves at lower frequencies (below 10 kHz). Utilising flexural waves for impact localisation requires a lower sampling frequency, conserving power and data storage, and facilitates TDOA extraction due to the dominance of flexural waves. Additionally, several studies have employed triangulation for impact localisation without considering the specific wave type, either by exploiting material isotropy [36] or estimating the WVP using TDOA data [37] or using signal energy as a complement to TDOA [38,39].

Given that modal-based, transfer function-based, and wave propagation-based methods all rely on physical information about the structure for impact localisation, data-driven methods offer a promising alternative by leveraging pre-collected training impact data alone. By establishing correlations between training impact sensor signals and their corresponding impact locations, an impact localisation model can be developed and applied to locate target impacts. Data-driven methods offer the advantage of being adaptable to complex structures without the need for detailed knowledge of material properties and boundary conditions [10,12], making them versatile and practical to locate impacts on complex composite structures.

Depending on the training features utilised for impact localisation, these data-driven methods can be straightforwardly categorised into TDOA-dependent data-driven [40–51] and TDOA-free data-driven methods [52–58]. Surrogate modelling is a straightforward technique for both TDOA-dependent and TDOA-free data-driven impact localisation. For example, Liu [53,54] investigated the employment of wavelet packet energy and multi-domain features for impact localisation using support vector regression. Damm [55] employed convolutional neural network (CNN) to localise impacts by inputting the short-time Fourier transform of sensor signals. Zhao [56] constructed a probabilistic neural network using features extracted by variational mode decomposition and multiscale permutation entropy. Sharif-Khodaei [47] developed an artificial neural network (ANN) to locate impacts on a stiffened composite panel using FEM training impact data with various input features. This study emphasised the effectiveness of TDOA extracted from sensor signals as an input feature for accurate impact localisation. Seno and Aliabadi [48–50] conducted low-mass, low-energy impact experiments on composite panels, varying impact angles, masses, impactor materials, and environmental temperatures. Localisation accuracy remained high under these diverse environmental and operational conditions, based on Kriging surrogate and TDOA extracted by the Normalized Smooth Envelope Threshold (NSET) method. Balasubramanian [41] conducted a comparative analysis of different neural network architectures, such as ANN, CNN, and Long Short-Term Memory network (LSTM), for accurate and robust impact localisation. The study revealed that ANN, utilising TDOA as a feature, demonstrated superior accuracy, while CNN showed greater robustness using sensor signals as inputs.

However, data-driven impact localisation methods relying on TDOA encounter shortcomings on two fronts. Firstly, the type and frequency components of the impact-induced waves used for TDOA extraction significantly influence impact localisation. Analysing the characteristics and extent of impact-induced waves is crucial, along with the development of precise and consistent TDOA extraction techniques. Secondly, data-driven impact localisation methods face challenges regarding their generalisability. Localisation accuracy beyond the training impact area can significantly deteriorate. While increasing the number of training impacts may enhance generalisability, it is often impractical due to the high costs associated with collecting extensive training data covering various impact scenarios.

To mitigate the costs associated with collecting training impact data, multi-fidelity modelling for SHM has drawn attention in recent years [59–61]. This approach allows for the utilisation of inexpensive low-fidelity training data, typically derived from analytical analyses or numerical simulations, to supplement or replace the need for expensive high-fidelity training data obtained from experiments. Seno [62] developed a multi-fidelity Co-Kriging surrogate for impact localisation by integrating numerical and experimental training impact data. This study demonstrates the feasibility of reducing the costs associated with collecting expensive experimental impact data by leveraging less costly numerical alternatives. Kalimullah [63] measured the wave velocity profile through active sensing experiments and incorporated this low-fidelity velocity profile information along with high-fidelity experimental impacts into a multi-fidelity ANN model using transfer learning techniques. However, in this study, the wave velocity profile was determined for non-dispersive extensional waves excited by active sensing. Given that extensional waves are highly contaminated by noise for impacts occurring far from the sensors, the TDOA of the experimental impacts was instead extracted from the dispersive flexural waves. The disparity between the low-fidelity velocity profile of the extensional waves and the TDOA of the flexural waves may lead to significant localisation errors, particularly for laminated composites with unbalanced laminate layers.

To enhance localisation accuracy beyond the training impact coverage area and reduce reliance on extensive training impact data, this study introduces a novel hybrid physics-based and data-driven (HPD) impact localisation method. This hybrid approach integrates the physical characteristics of impact-induced flexural waves into the localisation process, utilising a wave propagation velocity profile (WVP) governed by a dispersion equation derived analytically from equations of motion based on the first-order shear deformation theory (FSDT) [64]. The dispersion equation serves as a parameterisation method expressing the WVP as a function of material stiffness and wave frequency. Unlike conventional data-driven methods that approximate the WVP with a black box, this study explicitly formulates and optimises the WVP based on training impact data with respect to material stiffness and wave frequency. A two-stage approach is proposed for WVP optimisation, leveraging partial derivatives of the dispersion equation. This optimisation process only involves gradient-based optimisations such as Newton's method and the trust-region-reflective algorithm [65]. With the optimised velocity profile, triangulation is employed to locate the target impacts.

Experimental validation of the proposed HPD impact localisation method involves conducting impact testing on a composite laminate flat panel and a composite laminate stringer stiffened panel using a drop mass. Additionally, a data-driven method employing the ANN surrogate is utilised as a reference method, with the impact location uncertainty considered through 200 repetitions of the ANN training and testing process. A comparison of the localisation performance between the proposed HPD and ANN methods illustrates the ability of the HPD method to accurately localise impacts with minimal training impacts, even when impacts occur outside the training impact coverage area. Furthermore, impact tests on the stringer stiffened panel demonstrate the applicability of the proposed hybrid method for localising impact events on real in-service aircraft composite stiffened structures.

The subsequent sections of this paper are structured as follows. Section 2 presents the equations of motion of composite laminate plates, the dispersion relations of impact-induced waves (in-plane waves, out-of-plane flexural waves), the two-stage approach for optimising the WVP, the impact localisation by triangulation, and the TDOA extraction from the impact sensor signals. In Section 3, the experimental setup for impact testing on a composite laminate flat panel and a composite laminate stiffened panel is described. Sections 4 and 5 present the results of WVP optimisation and impact localisation for these two panels, respectively. The final conclusions are drawn in Section 6.

2. Methodology

The section commences with an introduction to the equations of motion governing composite laminate plates. These equations serve as the foundation for deriving and analysing the dispersion relations of both in-plane waves and out-of-plane flexural waves. Following this, the proposed hybrid physics-based and data-driven impact localisation approach is presented. This includes establishing the physical relationship between TDOA, wave velocity, and impact location, as well as optimising the WVP based on training impacts and dispersion relations. Moreover, the triangulation method for impact localisation utilising the optimised WVP is detailed. Finally, extracting TDOA from sensor signals is discussed.

2.1. Equations of motion of laminated composite plates

The structural equations of motion govern the impact-induced waves. These equations, specific to laminated composite plates, can be explicitly derived by applying classical laminate theory [66,67] in conjunction with plate theories [64], such as classical plate theory (CPT) and first-order shear deformation theory (FSDT), which simplify the shear strain along the plate thickness.

Since symmetrical laminates are predominantly used in most applications, this study focuses on symmetrically laminated plates, which is not considered a serious limitation. For a symmetrically laminated plate, neglecting body forces, the equations governing in-plane and out-of-plane motions in terms of displacements are outlined in Appendix A based on FSDT. These equations are employed to derive the dispersion relations of in-plane waves and out-of-plane flexural waves.

2.2. Non-dispersive impact-induced in-plane waves

For in-plane waves, assuming the harmonic waveform $u = Ue^{ik(r-ct)}$ and $v = Ve^{ik(r-ct)}$ with $r = x\cos\theta + y\sin\theta$, where k and c represent the wavenumber and the wave phase velocity in the θ direction, and substituting this waveform into Eq. (36), the governing equation for this harmonic waveform is formulated in matrix form:

$$\begin{aligned} &k^2\begin{bmatrix} C_{11}-I_1c^2 & C_{12} \\ C_{12} & C_{22}-I_1c^2 \end{bmatrix}\begin{bmatrix} U \\ V \end{bmatrix} = 0, \\ &C_{11} = A_{11}\cos^2\theta + A_{66}\sin^2\theta + 2A_{16}\sin\theta\cos\theta, \\ &C_{12} = A_{16}\cos^2\theta + A_{26}\sin^2\theta + (A_{12}+A_{66})\sin\theta\cos\theta, \\ &C_{22} = A_{66}\cos^2\theta + A_{22}\sin^2\theta + 2A_{26}\sin\theta\cos\theta. \end{aligned} \tag{1}$$

Here, $A_{ij}, i, j = 1, 2, 6$ represent laminate stiffness, as defined in Appendix A. $I_1 = \rho h$ denotes the mass per unit length, where ρ and h represent the density and thickness of the plate. For a non-trivial solution, the determinant of the coefficient matrix should be zero, resulting in the simplified dispersion equation in terms of wave velocity for non-zero wavenumber:

$$(C_{11}-I_1c^2)(C_{22}-I_1c^2) - C_{12}^2 = 0. \tag{2}$$

It can be observed that this is a biquadratic equation in terms of wave velocity c, which possesses an explicit analytical solution:

$$\begin{aligned} &c^2 = \frac{-C_b \pm \sqrt{C_b^2 - 4C_aC_c}}{2C_a},\ C_a = I_1^2, \\ &C_b = -I_1(C_{11}+C_{22}),\ C_c = C_{11}C_{22} - C_{12}^2. \end{aligned} \tag{3}$$

The operation $\pm$ indicate two wave modes with distinct phase velocities. These two phase velocities correspond precisely to the velocities of the in-plane extensional wave and the in-plane shear wave, with the in-plane extensional wave corresponding to the mode with the larger velocity value.

The phase velocity of in-plane waves, denoted by c, remains independent of the wavenumber k, indicating that in-plane waves exhibit nondispersive behaviour. This characteristic is ideally suited for impact localisation, as it implies that the wave velocity remains constant

regardless of the impact excitation or wave frequency. However, in practical impact scenarios, the in-plane deformation is typically negligible [31]. Even in cases of oblique 45-degree impacts, experimental evidence confirms that flexural waves predominate and the amplitude of the in-plane waves is dramatically small [30], especially when the impact is far away from the sensor. Such low amplitude allows the noise to significantly contaminate the identification of the in-plane waves from the sensor signals. Therefore, there is no necessity to further approximate displacement using higher-order plate theory to account for the dispersive properties of these in-plane waves.

2.3. Dispersive impact-induced flexural waves

In this subsection, the dispersion relations of the impact-induced flexural waves are first derived based on the governing equations of out-of-plane motion illustrated in Eq. (37). Subsequently, the wave modes and wave velocities are analysed. Finally, an example of flexural wave analysis in a laminated composite plate is presented.

2.3.1. Dispersion relations of the flexural waves

For flexural waves, assuming the harmonic waveform $w = We^{ik(r-ct)}$, $\psi_x = \Psi_x e^{ik(r-ct)}$, $\psi_y = \Psi_y e^{ik(r-ct)}$ with $r = x\cos\theta + y\sin\theta$, then substituting into the equations of out-of-plane motion Eq. (37), this waveform is governed by:

$$\mathbf{G}\begin{bmatrix} W \\ \Psi_x \\ \Psi_y \end{bmatrix} = \begin{bmatrix} g_{11} & g_{12} & g_{13} \\ g_{21} & g_{22} & g_{23} \\ g_{31} & g_{32} & g_{33} \end{bmatrix}\begin{bmatrix} W \\ \Psi_x \\ \Psi_y \end{bmatrix} = 0, \tag{4}$$

where W, Ψ_x, Ψ_y represent the wave amplitudes. The elements g_{ij}, for $i, j = 1, 2, 3$, of the coefficient matrix $\mathbf{G}$ are given by:

$$\begin{aligned}
g_{11} &= -(A_{44}\sin^2\theta + A_{55}\cos^2\theta + 2A_{45}\sin\theta\cos\theta)k^2 \\
&\quad + I_1 k^2 c^2, \\
g_{12} &= g_{21} = i(A_{55}\cos\theta + A_{45}\sin\theta)k, \\
g_{13} &= g_{31} = i(A_{45}\cos\theta + A_{44}\sin\theta)k, \\
g_{22} &= (D_{11}\cos^2\theta + 2D_{16}\sin\theta\cos\theta + D_{66}\sin^2\theta)k^2 \\
&\quad + A_{55} - I_3 k^2 c^2, \\
g_{23} &= g_{32} = [(D_{12} + D_{66})\sin\theta\cos\theta + D_{16}\cos^2\theta]k^2 \\
&\quad + D_{26}\sin^2\theta k^2 + A_{45}, \\
g_{33} &= (D_{22}\sin^2\theta + D_{66}\cos^2\theta + 2D_{26}\sin\theta\cos\theta)k^2 \\
&\quad + A_{44} - I_3 k^2 c^2,
\end{aligned} \tag{5}$$

where i denotes the imaginary unit ($i^2 = -1$). D_{ij} where $i, j = 1, 2, 6$, A_{ij} where $i, j = 4, 5$, represent laminate stiffness, as defined in Appendix A. $I_3 = \int_{-h/2}^{h/2} \rho z^2 dz$ is typically referred to as the rotational inertia. For a nontrivial solution, the determinant of the matrix $\mathbf{G}$ is zero:

$$\begin{aligned}
&g_{11}(g_{22}g_{33} - g_{23}^2) + g_{12}(g_{13}g_{23} - g_{12}g_{33}) \\
&\quad + g_{13}(g_{12}g_{23} - g_{13}g_{22}) = 0.
\end{aligned} \tag{6}$$

This dispersion equation is a sextic polynomial equation in terms of the phase velocity c, containing only even-degree terms. For each wavenumber k, there are three solutions to this equation for the phase velocity, corresponding to three values of angular frequency $\omega = ck$ and three wave modes. To evaluate the limit of Eq. (6) as the wavelength becomes infinite ($k \to 0$), the terms solely related to k are omitted, and ck is expressed by the angular frequency ω. The cut-off frequencies of these three wave modes are the solutions to:

$$I_1\omega^2[(A_{55} - I_3\omega^2)(A_{44} - I_3\omega^2) - A_{45}^2] = 0. \tag{7}$$

The solution $\omega_c = 0$ corresponds to the lowest mode of the flexural waves, which has a velocity of zero as $k \to 0$. Other two solutions ($\omega_c > 0$) represent two higher modes whose phase velocities become infinite as $k \to 0$.

It is worth noting that in the absence of shear modulus information, G_{23} and G_{13} are usually assumed to be equal to G_{12}. In this case, $G_{23} = G_{13}$ leads to $A_{44} = A_{55}$ and $A_{45} = 0$. From Eq. (7), the cutoff frequencies of these two higher modes are identically equal to $\sqrt{A_{44}/I_3}$. Due to the lack of information and for the sake of simplicity, the following analysis will adhere to the assumption that $G_{23} = G_{13} = G_{12}$. This assumption simplifies the $\mathbf{G}$ matrix (replacing k with ω/c) to:

$$\begin{aligned}
g_{11} &= -A_{44}\frac{\omega^2}{c^2} + I_1\omega^2, \\
g_{12} &= g_{21} = iA_{44}\frac{\omega}{c}\cos\theta, \\
g_{13} &= g_{31} = iA_{44}\frac{\omega}{c}\sin\theta, \\
g_{22} &= (D_{11}\cos^2\theta + 2D_{16}\sin\theta\cos\theta + D_{66}\sin^2\theta)\frac{\omega^2}{c^2} \\
&\quad + A_{44} - I_3\omega^2, \\
g_{23} &= g_{32} = [(D_{12} + D_{66})\sin\theta\cos\theta + D_{16}\cos^2\theta]\frac{\omega^2}{c^2} \\
&\quad + D_{26}\sin^2\theta\frac{\omega^2}{c^2}, \\
g_{33} &= (D_{22}\sin^2\theta + D_{66}\cos^2\theta + 2D_{26}\sin\theta\cos\theta)\frac{\omega^2}{c^2} \\
&\quad + A_{44} - I_3\omega^2.
\end{aligned} \tag{8}$$

2.3.2. Limiting velocities and monotonicity of the flexural waves

As the wavenumber/frequency tends to infinity, the phase velocities for these three wave modes approach constant values. Evaluating the limit of Eq. (6) when the frequency becomes infinite ($\omega \to +\infty$) by omitting the lower-order terms of ω except ω^6 results in an equation:

$$\omega^6\left(\frac{A_{44}}{c^2} - I_1\right)\left[\left(\frac{b_{22}}{c^2} - I_3\right)\left(\frac{b_{33}}{c^2} - I_3\right) - \frac{b_{23}^2}{c^2}\right] = 0. \tag{9}$$

These intermediate parameters b_{22}, b_{33} and b_{23} extracted from their corresponding g_{ij} are given by:

$$\begin{aligned}
b_{22} &= D_{11}\cos^2\theta + 2D_{16}\sin\theta\cos\theta + D_{66}\sin^2\theta, \\
b_{23} &= (D_{12} + D_{66})\sin\theta\cos\theta + D_{16}\cos^2\theta + D_{26}\sin^2\theta, \\
b_{33} &= D_{22}\sin^2\theta + D_{66}\cos^2\theta + 2D_{26}\sin\theta\cos\theta.
\end{aligned} \tag{10}$$

The velocity solution $\bar{c} = \sqrt{A_{44}/I_1} = \alpha\sqrt{G_{12}/\rho}$ from Eq. (9) represents the limiting phase velocity value of the lowest mode flexural waves as the frequency tends to infinity. This velocity is solely dependent on the shear modulus and density of the laminates. However, the limiting velocities of the other two higher modes also depend on the wave propagation direction θ. Specifically, in the $\theta = 0$ direction with $b_{22} = D_{11}$, $b_{23} = D_{16}$ and $b_{33} = D_{66}$, expanding the dispersion equation Eq. (6) yields:

$$\begin{aligned}
&\left[(D_{11}\frac{\omega^2}{c^2} + A_{44} - I_3\omega^2)(D_{66}\frac{\omega^2}{c^2} + A_{44} - I_3\omega^2) - (D_{16}\frac{\omega^2}{c^2})^2\right] \\
&\quad * (-A_{44}\frac{\omega^2}{c^2} + I_1\omega^2) \\
&\quad + A_{44}^2\frac{\omega^2}{c^2}(D_{66}\frac{\omega^2}{c^2} + A_{44} - I_3\omega^2) = 0.
\end{aligned} \tag{11}$$

The limiting velocities of the two higher modes in the $\theta = 0$ direction as the frequency approaches infinity are expressed as:

$$\begin{aligned}
\hat{c}^2 &= \frac{(D_{11}+D_{66})I_3 + D_{16}^2 \pm \sqrt{[(D_{11}+D_{66})I_3 + D_{16}^2]^2 - 4D_{11}D_{66}I_3^2}}{2I_3^2} \\
&\geq \min(D_{11}, D_{66})/I_3 \geq \frac{G_{12}}{\rho} > \bar{c}^2.
\end{aligned} \tag{12}$$

Consider a unidirectional lamina whose stiffness matrix $\bar{Q}_{ij}, i, j = 1, 2, 6$ is calculated based on the principal fibre orientation ($\phi = 0$), $\bar{Q}_{11}$ reaches its maximum ($\bar{Q}_{11} = Q_{11} = E_1/(1 - \nu_{12}\nu_{21})$), $\bar{Q}_{66}$ reaches it minimum ($\bar{Q}_{66} = Q_{66} = G_{12}$) and $\bar{Q}_{16}$ vanishes ($\bar{Q}_{16} = 0$). Consequently, the limiting velocity of one of the two higher modes takes its minimal value, which remains slightly larger than that of the lowest mode ($\bar{c} = \alpha\sqrt{G_{12}/\rho}$) as the frequency approaches infinity. Laminates with multiple pliers placed in different orientations increase the average stiffness D_{66} compared to a unidirectional laminate, resulting in a greater limiting velocity for higher modes. Varying the principal directions of the laminates from the fibre direction also increases the D_{66}. Since the rotations of principal directions of laminates ϕ are equivalent to the change of wave propagation direction θ in the dispersion equation concerning the calculation of phase velocity, the limiting velocities of the higher modes in every wave propagation direction exceed that of the lowest mode ($\bar{c} = \alpha\sqrt{G_{12}/\rho}$). Therefore, due to the nature of the laminates, $b_{22} > I_3\bar{c}^2 > 0$ and $b_{33} > I_3\bar{c}^2 > 0$ are maintained for all wave propagation directions θ since $\hat{c} \geq \bar{c}$. Furthermore, a simple

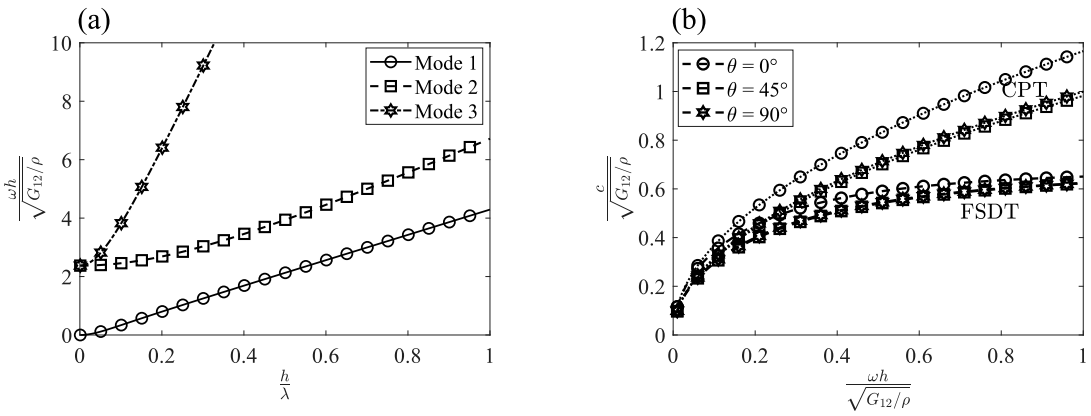


Fig. 1. The modes and velocities of flexural waves. (a) Spectrum relations depict the relationship between frequency ω and wavenumber k. For the three wave modes of flexural waves in the $\theta = 0$ direction, wave frequency increases with the wavenumber. The higher two modes initiate with non-zero cut-off frequencies. (b) Dispersion relations portray the relationship between wave velocity c and frequency ω. Comparing the wave velocity of the lowest mode at $\theta = 0°, 45°, 90°$ directions illustrates the positive relationship between velocity and frequency.

transformation on $(b_{22}/c^2 - I_3)(b_{33}/c^2 - I_3) - b_{23}^2/c^2 > 0$ demonstrates $g_{22}g_{33} - g_{23}^2 > 0$ if $c \in (0, \bar{c})$.

Intuitively, the phase velocity of the lowest mode of flexural waves increases monotonically with frequency and is bounded in $(0, \bar{c})$. To prove this, assuming $c \in (0, \bar{c})$, the first-order partial derivative of wave velocity with respect to frequency, $\frac{\partial c}{\partial \omega}$, should be positive. Typically, D_{16} in Eq. (11) is relatively small, which does not influence the sign of $\frac{\partial c}{\partial \omega}$, especially for symmetric cross-ply laminates ($D_{16} = 0$). By disregarding D_{16}, Eq. (11) can be reformulated as:

$$\begin{aligned} &g_{11}g_{22} - g_{12}^2 = 0,\ g_{11} = -A_{44}\frac{\omega^2}{c^2} + I_1\omega^2, \\ &g_{22} = D_{11}\frac{\omega^2}{c^2} + A_{44} - I_3\omega^2,\ g_{12} = iA_{44}\frac{\omega}{c}. \end{aligned} \tag{13}$$

The derivative of wave velocity with respect to frequency is calculated as:

$$\frac{\partial c}{\partial \omega} = \frac{c}{\omega}\frac{g_{11}(g_{22} - A_{44})}{g_{11}(g_{22} - A_{44} + I_3\omega^2) - g_{22}I_1\omega^2} > 0. \tag{14}$$

When $c \in (0, \bar{c})$, g_{11} is negative. Moreover, given that $b_{22} = D_{11} > I_3\bar{c}^2 > 0$, g_{22} exceeds A_{44}. Consequently, both the numerator and denominator in Eq. (14) are negative, resulting in a positive derivative. This confirms the monotonically increasing relationship between the phase velocity of the lowest-mode flexural waves and the frequency.

It can be observed from Eqs. (6) and (11) that the phase velocity of flexural waves varies with the wavenumber/frequency. Particularly for the lowest mode, as the wavenumber (or frequency) increases, the phase velocity also increases, indicating the dispersive nature of flexural waves. Although Eq. (6) describes these dispersion relations, there is no explicit algebraic solution to this dispersion equation. However, approximate numerical solutions for the wave velocity of the lowest mode can be obtained for any wavenumber or frequency using methods such as the bisection method or Newton's method, as the phase velocity c of the lowest-mode flexural waves, bounded within the range $(0, \bar{c})$, monotonically increases with frequency.

2.3.3. Example of flexural wave analysis in a laminated composite plate

To demonstrate the dispersive nature of flexural waves, an analysis was conducted on flexural wave propagation in a symmetric cross-ply laminate with a layup of $[0/90]_{4s}$. The material properties of the unidirectional ply are outlined in Table 1. Fig. 1(a) illustrates the spectrum relations, which portray the relationship between frequency and wavenumber, for the three modes of flexural waves in the $\theta = 0$ direction. In this illustration, the wavenumber k and frequency ω are nondimensionalised by the laminate thickness h and velocity $\sqrt{G_{12}/\rho}$, respectively.

As the wavenumber k increases, the frequency of the flexural wave modes also rises. For a specific wavenumber k, the higher mode corresponds to a greater frequency ω (or a higher phase velocity c). This nonlinear relationship between frequency and wavenumber underscores the dispersive nature of flexural waves.

Table 1
Material properties of a unidirectional lamina (M21/T800s)

Property	E_1 [MPa]	E_2 [MPa]	G_{12} [MPa]	ν_{12}	ρ [g/mm^3]
Value	171000	11470	4830	0.3	1.6e−3

*E_1: elastic modulus in the fibre direction, E_2: elastic modulus perpendicular to the fibre direction, G_{12}: shear modulus, ν_{12}: Poisson's ratio, ρ: density.

To further explore the behaviour of the lowest wave mode, which is the focus of this study, dispersion relations (plots of phase velocity as a function of frequency, $c = dr(\omega)$) are depicted in Fig. 1(b). These relations include velocity comparisons between CPT and FSDT for wave propagation directions of 0, 45, and 90 degrees.

As frequency increases, phase velocities also increase in all directions, indicating a monotonically increasing relationship and confirming the dispersive property of flexural waves. Additionally, it is observed that CPT tends to overestimate wave velocity compared to FSDT due to its neglect of shear deformation and rotational inertia effects. However, for low wave frequencies, CPT can serve as an approximation of FSDT for phase velocity calculations. The dispersion relations for flexural waves based on CPT are derived in Appendix B, where phase velocity increases linearly with the square root of frequency and is unbounded.

It is important to note that waves correspond to specific types of motion. In impact dynamics, flexural (bending) motions predominate, while twisting is negligible. In the three governing equations of out-of-plane motions derived based on FSDT, as shown in Eq. (37), the rotational terms are employed to describe shear deformations, which are coupled with and contribute to the dominant out-of-plane flexural motions. Therefore, the study does not consider possible torsional waves (negligible) induced by rotational terms. The derived dispersion relations govern the flexural waves, which are dominant and of primary interest in this study.

2.4. Dispersion relations explicitly parameterise the velocity of impact-induced flexural waves

The focus of this study lies on the lowest mode of flexural waves, which carries the majority of impact-induced wave energy, particularly when the dominant frequency of the impact-induced waves is lower than the cut-off frequency. Referring back to Eq. (6), the parameters in this dispersion equation can be categorised into four groups: material stiffness A_{44} and D_{ij} where $i, j = 1, 2, 6$, wave frequency ω, flexural wave propagation angle θ, and flexural wave propagation

velocity c. Modifying the material stiffness or the wave frequency alters the wave velocity profile $c(\theta)$ accordingly. Naturally, this equation serves as a parameterisation method for the velocity profile of impact-induced flexural waves. Assuming independence of the material stiffness, the independent design variables of this parameterisation method for the wave velocity profile amount to eight in total: $\mathbf{x} = (D_{11}, D_{12}, D_{16}, D_{22}, D_{26}, D_{66}, A_{44}, \omega)$. The first-order partial derivative of wave velocity with respect to the nth design variable is derived from this dispersion equation Eq. (6) as:

$$\begin{aligned}&(g_{22}g_{33} - g_{23}^2)\frac{\partial g_{11}}{\partial x_n} + (g_{11}g_{33} - g_{13}^2)\frac{\partial g_{22}}{\partial x_n}\\ &+ (g_{11}g_{22} - g_{12}^2)\frac{\partial g_{33}}{\partial x_n} + 2(g_{13}g_{23} - g_{12}g_{33})\frac{\partial g_{12}}{\partial x_n}\\ &+ 2(g_{12}g_{23} - g_{13}g_{22})\frac{\partial g_{13}}{\partial x_n} + 2(g_{12}g_{13} - g_{11}g_{23})\frac{\partial g_{23}}{\partial x_n} = 0.\end{aligned} \tag{15}$$

For simplification purposes, defining a_{ij}, where $i, j = 1, 2, 3$, as the leading principal minors of matrix $\mathbf{G}$:

$$\begin{aligned}&a_{11} = g_{22}g_{33} - g_{23}^2,\ a_{22} = g_{11}g_{33} - g_{13}^2,\\ &a_{33} = g_{11}g_{22} - g_{12}^2,\ a_{12} = g_{13}g_{23} - g_{12}g_{33},\\ &a_{13} = g_{12}g_{23} - g_{13}g_{22},\ a_{23} = g_{12}g_{13} - g_{11}g_{23},\end{aligned} \tag{16}$$

the dispersion equation $det(\mathbf{G}) = 0$ can be formulated using Laplace expansion from the ith row or the jth column:

$$\begin{aligned}det(\mathbf{G}) &= \sum_{j=1}^{3} a_{ij}g_{ij}|_{i=1,2,3}\\ &= \sum_{i=1}^{3} a_{ij}g_{ij}|_{j=1,2,3} = 0.\end{aligned} \tag{17}$$

Meanwhile, its first-order partial derivative, as shown in Eq. (15), can be rearranged with $a_{ij}, i, j = 1, 2, 3$ as:

$$\begin{aligned}&a_{11}\frac{\partial g_{11}}{\partial x_n} + a_{22}\frac{\partial g_{22}}{\partial x_n} + a_{33}\frac{\partial g_{33}}{\partial x_n}\\ &+ 2a_{12}\frac{\partial g_{12}}{\partial x_n} + 2a_{13}\frac{\partial g_{13}}{\partial x_n} + 2a_{23}\frac{\partial g_{23}}{\partial x_n} = 0.\end{aligned} \tag{18}$$

The second-order partial derivatives of the dispersion equation with respect to variables x_n and x_m, are further derived as:

$$\begin{aligned}&\frac{\partial a_{11}}{\partial x_m}\frac{\partial g_{11}}{\partial x_n} + a_{11}\frac{\partial^2 g_{11}}{\partial x_n \partial x_m} + \frac{\partial a_{22}}{\partial x_m}\frac{\partial g_{22}}{\partial x_n} + a_{22}\frac{\partial^2 g_{22}}{\partial x_n \partial x_m}\\ &+ \frac{\partial a_{33}}{\partial x_m}\frac{\partial g_{33}}{\partial x_n} + a_{33}\frac{\partial^2 g_{33}}{\partial x_n \partial x_m} + 2(\frac{\partial a_{12}}{\partial x_m}\frac{\partial g_{12}}{\partial x_n} + a_{12}\frac{\partial^2 g_{12}}{\partial x_n \partial x_m})\\ &+ 2(\frac{\partial a_{13}}{\partial x_m}\frac{\partial g_{13}}{\partial x_n} + a_{13}\frac{\partial^2 g_{13}}{\partial x_n \partial x_m}) + 2(\frac{\partial a_{23}}{\partial x_m}\frac{\partial g_{23}}{\partial x_n} + a_{23}\frac{\partial^2 g_{23}}{\partial x_n \partial x_m}) = 0.\end{aligned} \tag{19}$$

Here is an example to illustrate the calculation of the first-order partial derivative $\frac{\partial c}{\partial \omega}$. By letting $x_n = \omega$ in Eq. (18), the first-order partial derivatives of g_{ij}, where $i, j = 1, 2, 3$, with respect to the frequency ω are:

$$\begin{aligned}\frac{\partial g_{11}}{\partial \omega} &= -2A_{44}[\frac{\omega}{c^2} - \frac{\omega^2}{c^3}\frac{\partial c}{\partial \omega}] + 2I_1\omega,\\ \frac{\partial g_{22}}{\partial \omega} &= 2b_{22}(\frac{\omega}{c^2} - \frac{\omega^2}{c^3}\frac{\partial c}{\partial \omega}) - 2I_3\omega,\\ \frac{\partial g_{33}}{\partial \omega} &= 2b_{33}(\frac{\omega}{c^2} - \frac{\omega^2}{c^3}\frac{\partial c}{\partial \omega}) - 2I_3\omega,\\ \frac{\partial g_{12}}{\partial \omega} &= iA_{44}\cos\theta(\frac{1}{c} - \frac{\omega}{c^2}\frac{\partial c}{\partial \omega}),\\ \frac{\partial g_{13}}{\partial \omega} &= iA_{44}\sin\theta(\frac{1}{c} - \frac{\omega}{c^2}\frac{\partial c}{\partial \omega}),\\ \frac{\partial g_{23}}{\partial \omega} &= 2b_{23}(\frac{\omega}{c^2} - \frac{\omega^2}{c^3}\frac{\partial c}{\partial \omega}).\end{aligned} \tag{20}$$

Substituting $\frac{\partial g_{ij}}{\partial \omega}, i, j = 1, 2, 3$ into Eq. (18), $\frac{\partial c}{\partial \omega}$ is derived in combination with Eq. (17) as:

$$\frac{\partial c}{\partial \omega} = \frac{a_{11}g_{11} - (a_{22}+a_{33})A_{44}}{-a_{11}A_{44}\frac{\omega^2}{c^2} - (a_{22}+a_{33})(A_{44} - I_3\omega^2)}\frac{c}{\omega}. \tag{21}$$

2.5. Physical relation correlates impact location, TDOA, and wave velocity

To integrate the dispersion relations of lowest-mode flexural waves into impact localisation, the physical relation between impact location, TDOA and wave propagation velocity is established as:

$$\begin{aligned}\Delta t_{ij} &= t_j - t_i = \frac{d_j}{c(\theta_j)} - \frac{d_i}{c(\theta_i)}\\ &= \frac{\sqrt{(x_s - x_j)^2 + (y_s - y_j)^2}}{c(\theta_j)} - \frac{\sqrt{(x_s - x_i)^2 + (y_s - y_i)^2}}{c(\theta_i)},\end{aligned} \tag{22}$$

where (x_s, y_s) denotes the impact location (source), (x_i, y_i) and (x_j, y_j) represent the locations of the ith and jth sensors, and $c(\theta_i)$ and $c(\theta_j)$ are the impact-induced wave propagation velocities along the paths from the impact to the ith and jth sensors, respectively. Hence, given the WVP and the sensor locations, the impact location can be estimated using TDOA data.

In practice, TDOA data are extracted from the signals recorded by passive sensors. Widely-used data-driven methods for impact localisation involve constructing a model, often through techniques such as surrogate modelling [68] or recursive filter estimation [69], which establishes a relationship between these TDOA values and the impact location based on training impacts. Essentially, these methods approximate the WVP and the sensor locations using a black-box function, facilitating the estimation of the impact location. However, these data-driven approaches heavily rely on the TDOA extraction method, which must consistently extract TDOA values from the same wave frequency component across various impact scenarios.

Moreover, since the locations of sensors are also estimated during the training process, any errors in the estimation of sensor locations significantly impact the accuracy of the approximated velocity profile, particularly when training impact data are limited. Consequently, data-driven methods for impact localisation typically require a large volume of training impact data and may struggle to accurately locate impacts outside the coverage area of the training impacts.

Instead of relying on a black-box surrogate model to approximate the WVP, this study explicitly optimises the WVP parameterised by material stiffness and wave frequency as detailed in Section 2.4, using training impact data. During this optimisation process, sensor location information is integrated into the objective function, resulting in a more accurate estimation of the WVP. As the wave frequency on which the TDOA extraction is based cannot be determined exactly, the frequency ω serves as an optimisation design variable. By utilising the optimised WVP, the location of the target impact is determined using the triangulation method, which minimises the discrepancy between the estimated TDOA from the optimised WVP and the extracted TDOA from sensor signals. The localisation uncertainty can be further estimated based on this discrepancy.

It is noteworthy that in this study, the WVP is parameterised by a total of eight design variables ($\mathbf{x} = (D_{11}, D_{12}, D_{16}, D_{22}, D_{26}, D_{66}, A_{44}, \omega)$), which is significantly smaller than that of conventional surrogate modelling methods. For example, the number of parameters to be optimised in ANN can easily exceed several hundred, depending on the number of neural network layers and the number of neurons in each layer.

The objective function R (objective residual) for optimising the WVP based on the training impacts is defined as the sum of squared errors between the estimated and actual TDOA values. Therefore, this optimisation problem can be expressed as:

$$\begin{aligned}&\mathbf{x} = (D_{11}, D_{12}, D_{16}, D_{22}, D_{26}, D_{66}, A_{44}, \omega),\\ &\mathbf{x}_{opt} = \arg\min_{\mathbf{x}} R = \arg\min_{\mathbf{x}} \sum_{i=1}^{N_i}\sum_{j=2}^{N_s} r^2,\\ &r = (\frac{d_{ij}}{c(\theta_{ij};\omega)} - \frac{d_{i1}}{c(\theta_{i1};\omega)}) - \Delta t_{1j}^i,\\ &c_{opt}(\theta) = c(\theta; \mathbf{x}_{opt}),\end{aligned} \tag{23}$$

where r represents the difference between the estimated and actual TDOA, N_i and N_s are the number of training impacts and sensors, respectively. d_{ij} and θ_{ij} denote the known distance and wave propagation direction from the ith training impact to jth sensor, respectively. $c(\theta_{ij}; \mathbf{x})$ represents the wave propagation velocity along the direction θ_{ij} given the parameters $\mathbf{x}$ obtained by solving Eq. (6). In the definition of objective residual for minimisation, sensor 1 is designated as the anchor sensor. TDOA are calculated between sensor $j, j \geq 2$ and sensor 1. Therefore, $\Delta t_{1j}^i = t_j^i - t_1^i$ represents the known actual TDOA between sensor $j, j \geq 2$ and sensor 1 for ith training impact.

2.6. Wave velocity profile optimisation: A two-stage approach

The optimisation of the WVP, as depicted in Eq. (23), can be achieved through heuristic optimisation algorithms such as Genetic Algorithms (GA). However, solving this eight-dimensional optimisation problem using GA necessitates a substantial number of objective function evaluations, making the process time-consuming. Moreover, enhancing the wave propagation velocity can be achieved by either adjusting the design variables associated with stiffness $A_{44}, D_{ij}, i, j = 1, 2, 6$ or by augmenting the wave frequency ω. Since these stiffness are intrinsic material properties, which are typically approximately known beforehand, it is preferable to scale the wave velocity by optimising the wave frequency ω and fine-tune the shape of the WVP by optimising the stiffness $A_{44}, D_{ij}, i, j = 1, 2, 6$ within their confidence regions. Therefore, a two-stage approach is proposed to address this WVP optimisation problem.

2.6.1. Stage 1: Scale the WVP by optimising the wave frequency ω

To scale the WVP by optimising the wave frequency ω, the first-order and second-order partial derivatives of objective residual R with respect to the frequency ω are derived using the chain rule. This first-order partial derivative $\frac{\partial R}{\partial \omega}$ is derived as:

$$\begin{aligned}\frac{\partial R}{\partial \omega} &= \frac{\partial \sum_{i=1}^{N_i}\sum_{j=2}^{N_s} r^2}{\partial \omega} = \sum_{i=1}^{N_i}\sum_{j=2}^{N_s} 2r\frac{\partial r}{\partial \omega} \\ &= 2\sum_{i=1}^{N_i}\sum_{j=2}^{N_s} r(\frac{\partial r}{\partial c}\cdot\frac{\partial c}{\partial \omega}), \\ \frac{\partial r}{\partial c} &= [-\frac{d_{ij}}{c^2(\theta_{ij};\omega)}, \frac{d_{i1}}{c^2(\theta_{i1};\omega)}], \ \frac{\partial c}{\partial \omega} = [\frac{\partial c(\theta_{ij};\omega)}{\partial \omega}, \frac{\partial c(\theta_{i1};\omega)}{\partial \omega}],\end{aligned} \tag{24}$$

where $\cdot$ represents the dot product operation. Both $\frac{\partial r}{\partial c}$ and $\frac{\partial c}{\partial \omega}$ are vectors with 2 elements, as r is related to c in both θ_{ij} and θ_{i1} directions. The second-order partial derivative of the objective residual R with respect to the frequency ω is further derived as:

$$\begin{aligned}\frac{\partial^2 R}{\partial \omega^2} &= 2\sum_{i=1}^{N_i}\sum_{j=2}^{N_s}(\frac{\partial r}{\partial c}\cdot\frac{\partial c}{\partial \omega})^2 + r[\frac{\partial^2 r}{\partial c^2}\cdot(\frac{\partial c}{\partial \omega})^2 + \frac{\partial r}{\partial c}\cdot\frac{\partial^2 c}{\partial \omega^2}], \\ \frac{\partial^2 r}{\partial c^2} &= 2[\frac{d_{ij}}{c^3(\theta_{ij};\omega)}, -\frac{d_{i1}}{c^3(\theta_{i1};\omega)}], \ \frac{\partial^2 c}{\partial \omega^2} = [\frac{\partial^2 c(\theta_{ij};\omega)}{\partial \omega^2}, \frac{\partial^2 c(\theta_{i1};\omega)}{\partial \omega^2}].\end{aligned} \tag{25}$$

The dependence of the second-order partial derivatives $\frac{\partial^2 R}{\partial \omega^2}$ on the TDOA Δt^i_{1j} in r is noted. The convexity of the objective residual R with respect to the frequency ω remains uncertain. Utilising the Newton's method for optimisation based solely on these derivatives may lead to convergence to a local minimum.

Given that the frequency ω predominantly controls the scaling of the WVP, transitioning from ω_1 to ω_2 scales the velocity profile from $c_1(\theta)$ to $c_2(\theta)$. This scaling can be approximated by a velocity scale factor β, where $c_2(\theta)$ is approximately $c_1(\theta)/\beta$. Therefore, instead of optimising the frequency ω, the velocity scale factor β can also be employed to scale the WVP to best align with the training impact locations and TDOA data. With ω_b held constant, the baseline velocity profile calculated from Eq. (6) is denoted as $c_b(\theta)$, maintaining a constant value for each wave propagation direction θ. The optimisation of the objective residual R with respect to velocity scale factor β is expressed as follows:

$$\begin{aligned}\beta_{opt} &= \arg\min_{\beta} R \\ &= \arg\min_{\beta} \sum_{i=1}^{N_i}\sum_{j=2}^{N_s}[(\frac{d_{ij}}{c_b(\theta_{ij})} - \frac{d_{i1}}{c_b(\theta_{i1})})\beta - \Delta t^i_{1j}]^2.\end{aligned} \tag{26}$$

The first and second-order partial derivatives of the objective residual R with respect to β are derived as follows:

$$\begin{aligned}\frac{dR}{d\beta} &= 2\sum_{i=1}^{N_i}\sum_{j=2}^{N_s}[(\frac{d_{ij}}{c_b(\theta_{ij})} - \frac{d_{i1}}{c_b(\theta_{i1})})\beta - \Delta t^i_{1j}](\frac{d_{ij}}{c_b(\theta_{ij})} - \frac{d_{i1}}{c_b(\theta_{i1})}), \\ \frac{d^2 R}{d\beta^2} &= 2\sum_{i=1}^{N_i}\sum_{j=2}^{N_s}(\frac{d_{ij}}{c_b(\theta_{ij})} - \frac{d_{i1}}{c_b(\theta_{i1})})^2 \geq 0.\end{aligned} \tag{27}$$

As the second-order partial derivatives of the objective residual with respect to β are non-negative, this optimisation problem is convex, allowing for efficient solution using methods like the steepest descent or Newton's method. The Newton's method iteratively minimises R with respect to β:

$$\beta_{k+1} = \beta_k - \frac{R'(\beta_k)}{R''(\beta_k)}. \tag{28}$$

The optimised β_{opt} can then be utilised to update the frequency ω_b and adjust the velocity profile baseline $c_b(\theta)$ using the inverse dispersion relations $\omega = idr(c)$. These relations are derived from the dispersion relations $c = dr(\omega)$ illustrated in Fig. 1. The inverse dispersion relations represent a monotonic increasing function between wave frequency and phase velocity. The updates for the frequency ω_b and velocity profile baseline $c_b(\theta)$ are given by:

$$\omega_b = idr(c_b(\theta;\omega_b)/\beta_{opt}), \ c_b(\theta) = c(\theta;\omega_b). \tag{29}$$

Repeating such a convex optimisation with respect to the velocity scale factor β, and the update processes of the frequency ω_b and the velocity profile baseline $c_b(\theta)$ indirectly lead to the optimisation of the WVP and the identification of the optimal frequency. The pseudocode for this indirect optimisation approach is illustrated in Algorithm 1.

Algorithm 1: An indirect algorithm to optimise WVP with respect to frequency ω using the Newton's method

Input: $E_1, E_2, G_{12}, \nu_{12}, \rho, \boldsymbol{\Phi}, Ixy, Sxy, \Delta t^i_{1j}$
Output: ω_{opt}
$d_{ij}, \theta_{ij} \leftarrow Ixy, Sxy$;
$D, A \leftarrow E_1, E_2, G_{12}, \nu_{12}, \rho, \boldsymbol{\Phi}$;
$\omega_b \leftarrow 2\pi f_{NSET}$;
$\beta_{opt} \leftarrow 2$;
while $| \beta_{opt} - 1 | \geq 0.01$ **do**
  $c_b(\theta) \leftarrow c(\theta;\omega_b)$;
  $R \leftarrow \sum_{i=1}^{N_i}\sum_{j=2}^{N_s}[(\frac{d_{ij}}{c_b(\theta_{ij})} - \frac{d_{i1}}{c_b(\theta_{i1})})\beta - \Delta t^i_{1j}]^2$;
  $\beta_0 \leftarrow 1$;
  $\beta_{opt} \leftarrow \arg\min_{\beta} R$; /* Solve Eq. (26) by Newton's method */
  $\omega_b \leftarrow idr(c_b(\theta;\omega_b)/\beta_{opt})$;
end
$\omega_{opt} \leftarrow \omega_b$;

*$\boldsymbol{\Phi}$: laminate layup; Ixy: training impact locations; Sxy: sensors' locations; Δt^i_{1j}: training TDOA; f_{NSET}: cut-off frequency used for TDOA extraction.

2.6.2. Stage 2: Fine-tune the WVP by optimising the stiffness

The amplitude of the WVP, optimised with respect to the frequency, closely approximates its real value. Next, the shape of the WVP can be fine-tuned by minimising the objective residual with respect to the stiffness matrix D (where D represents $D_{11}, D_{12}, D_{16}, D_{22}, D_{26}, D_{66}$) and the stiffness A_{44} constrained within its confidence region. This second-stage optimisation problem is formulated as:

$$\begin{aligned}&D^{opt}, A^{opt}_{44} = \arg\min_{D,A_{44}} R = \arg\min_{D,A_{44}} \sum_{i=1}^{N_i}\sum_{j=2}^{N_s} r^2, \\ &r = (\frac{d_{ij}}{c(\theta_{ij};\, D, A_{44}, \omega_{opt})} - \frac{d_{i1}}{c(\theta_{i1};\, D, A_{44}, \omega_{opt})}) - \Delta t^i_{1j}, \\ &c_{opt}(\theta) = c(\theta;\, D^{opt}, A^{opt}_{44}, \omega_{opt}).\end{aligned} \tag{30}$$

To circumvent the use of the time-consuming GA for solving this seven-dimensional optimisation task, the trust-region-reflective algorithm [65] is employed. This method leverages the information from the partial derivatives of the objective residual with respect to the design variables (stiffness D, A_{44}). Through the chain rule, the first and second-order partial derivatives $\frac{\partial R}{\partial x_n}$ and $\frac{\partial^2 R}{\partial x_n \partial x_m}$ of the objective residual R with respect to the stiffness variable $x_n, x_m \in (D, A_{44})$ are deduced and expressed using intermediate derivatives $\frac{\partial r}{\partial c}$, $\frac{\partial^2 r}{\partial c^2}$, $\frac{\partial c}{\partial x_n}$, and $\frac{\partial^2 c}{\partial x_n \partial x_m}$:

$$\begin{aligned}\frac{\partial R}{\partial x_n} &= \sum_{i=1}^{N_i}\sum_{j=2}^{N_s} 2r\frac{\partial r}{\partial x_n} = 2\sum_{i=1}^{N_i}\sum_{j=2}^{N_s} r(\frac{\partial r}{\partial c}\cdot\frac{\partial c}{\partial x_n}), \\ \frac{\partial^2 R}{\partial x_n \partial x_m} &= 2\sum_{i=1}^{N_i}\sum_{j=2}^{N_s}\{(\frac{\partial r}{\partial c}\cdot\frac{\partial c}{\partial x_n})(\frac{\partial r}{\partial c}\cdot\frac{\partial c}{\partial x_m}) \\ &\quad + r[\frac{\partial^2 r}{\partial c^2}\cdot(\frac{\partial c}{\partial x_n}\frac{\partial c}{\partial x_m}) + \frac{\partial r}{\partial c}\cdot\frac{\partial^2 c}{\partial x_n \partial x_m}]\}.\end{aligned} \tag{31}$$

Algorithm 2: Trust-region-reflective algorithm to optimise WVP with respect to stiffness (D, A_{44})

Input: $E_1, E_2, G_{12}, \nu_{12}, \Phi, Ixy, Sxy, \Delta t_{ij}, \omega_{opt}$
Output: $c_{opt}(\theta)$
$d_{ij}, \theta_{ij} \leftarrow Ixy, Sxy$;
$D^0, A_{44}^0 \leftarrow E_1, E_2, G_{12}, \nu_{12}, \Phi$;
$[D^{lb}, D^{ub}] \leftarrow D^0, [A_{44}^{lb}, D_{44}^{ub}] \leftarrow A_{44}^0$;
$N_{iter} \leftarrow 10000, i_{iter} \leftarrow 1$;
$D \leftarrow D^0, A_{44} \leftarrow A_{44}^0$;
$r \leftarrow (\frac{d_{ij}}{c(\theta_{ij};\, D, A_{44}, \omega_{opt})} - \frac{d_{i1}}{c(\theta_{i1};\, D, A_{44}, \omega_{opt})}) - \Delta t_{1j}^i$;
$R \leftarrow \sum_{i=1}^{N_i} \sum_{j=2}^{N_s} r^2$;
$\Delta R \leftarrow 1, \Delta x \leftarrow 1$;
while $i_{iter} \le N_{iter}$ & $\Delta R > 10^{-6}$ & $\Delta x > 10^{-6}$ **do**
  $\frac{\partial c}{\partial x_n} \leftarrow D, A_{44}, \omega_{opt}$;
  $\frac{\partial R}{\partial x_n} \leftarrow \frac{\partial c}{\partial x_n}$;
  $[\delta D, \delta A_{44}] \leftarrow R, \frac{\partial R}{\partial x_n}$;
  $p \leftarrow R, \frac{\partial R}{\partial x_n}$;
  $[D, A_{44}] \leftarrow [D, A_{44}] - p[\delta D, \delta A_{44}]$;
  $r \leftarrow (\frac{d_{ij}}{c(\theta_{ij};\, D, A_{44}, \omega_{opt})} - \frac{d_{i1}}{c(\theta_{i1};\, D, A_{44}, \omega_{opt})}) - \Delta t_{1j}^i$;
  $\Delta R \leftarrow R - \sum_{i=1}^{N_i} \sum_{j=2}^{N_s} r^2$;
  $R \leftarrow \sum_{i=1}^{N_i} \sum_{j=2}^{N_s} r^2$;
  $\Delta x \leftarrow norm(p[\delta D, \delta A_{44}])$;
  $i_{iter} \leftarrow i_{iter} + 1$;
end
$D_{opt} \leftarrow D, A_{44}^{opt} \leftarrow A_{44}$;
$c(\theta) \leftarrow c(\theta;\, D_{opt}, A_{44}^{opt}, \omega_{opt})$;

*N_{iter}: Maximal number of iteration; ΔR: objective residual reduction; Δx: iterative change of design variables; p: updating step size, $[\delta D, \delta A_{44}]$: updating direction.

Algorithm 3: Triangulation method to locate impacts based on the optimised WVP

Input: $D_{opt}, A_{44}^{opt}, \omega_{opt}$
Input: $Sxy(x_j, y_j), \Delta t_{1j}, j = 1, 2, ..., N_s$
Input: $[x_{lb}, x_{ub}], [y_{lb}, y_{ub}]$
Output: x, y, σ_{xy}
$c(\theta) \leftarrow D_{opt}, A_{44}^{opt}, \omega_{opt}$;
$x, y \leftarrow \Delta t_{1j}$; /* Initial impact locations */
$d_j, \theta_j \leftarrow x, y, x_j, y_j$;
$R \leftarrow \sum_{j=2}^{N_s} [(\frac{d_j}{c(\theta_j)} - \frac{d_1}{c(\theta_1)}) - \Delta t_{1j}]^2$;
$N_{iter} \leftarrow 10000, i_{iter} \leftarrow 1$;
$\Delta R \leftarrow 1, \Delta x \leftarrow 1$;
while $i_{iter} \le N_{iter}$ & $\Delta R > 10^{-6}$ & $\Delta x > 10^{-6}$ **do**
  $\frac{\partial c(\theta_j)}{\partial x}, \frac{\partial c(\theta_j)}{\partial y} \leftarrow D_{opt}, A_{44}^{opt}, \omega_{opt}$;
  $\frac{\partial^2 c(\theta_j)}{\partial x^2}, \frac{\partial^2 c(\theta_j)}{\partial y^2}, \frac{\partial^2 c(\theta_j)}{\partial x \partial y} \leftarrow \frac{\partial c(\theta_j)}{\partial x}, \frac{\partial c(\theta_j)}{\partial y}$;
  $\frac{\partial R}{\partial x}, \frac{\partial R}{\partial y}, \frac{\partial^2 R}{\partial x^2}, \frac{\partial^2 R}{\partial y^2}, \frac{\partial^2 R}{\partial x \partial y} \leftarrow c(\theta)$;
  $[\delta x, \delta y] \leftarrow R, \frac{\partial R}{\partial x}, \frac{\partial R}{\partial y}, \frac{\partial^2 R}{\partial x^2}, \frac{\partial^2 R}{\partial y^2}, \frac{\partial^2 R}{\partial x \partial y}$;
  $p \leftarrow R, \frac{\partial R}{\partial x}, \frac{\partial R}{\partial y}, \frac{\partial^2 R}{\partial x^2}, \frac{\partial^2 R}{\partial y^2}, \frac{\partial^2 R}{\partial x \partial y}$;
  $[x, y] \leftarrow [x, y] - p[\delta x, \delta y]$;
  $d_j, \theta_j \leftarrow x, y, x_j, y_j$;
  $\Delta R \leftarrow R - \sum_{j=2}^{N_s} [(\frac{d_j}{c(\theta_j)} - \frac{d_1}{c(\theta_1)}) - \Delta t_{1j}]^2$;
  $R \leftarrow \sum_{j=2}^{N_s} [(\frac{d_j}{c(\theta_j)} - \frac{d_1}{c(\theta_1)}) - \Delta t_{1j}]^2$;
  $\Delta d \leftarrow norm(p[\delta x, \delta y])$;
  $i_{iter} \leftarrow i_{iter} + 1$;
end
$\sigma_{xy} \leftarrow x, y, c(\theta), \Delta t_{j1}$;

*$[x, y]$: estimated location of target impact; σ_{xy}:localisation uncertainty; $[x_{lb}, x_{ub}], [y_{lb}, y_{ub}]$: bounds of impact location determined by plate size.

Drawing from Eqs. (17), (18), and (19), the intermediate partial derivatives $\frac{\partial r}{\partial c}$, $\frac{\partial^2 r}{\partial c^2}$, $\frac{\partial c}{\partial x_n}$, and $\frac{\partial^2 c}{\partial x_n \partial x_m}$ can be derived analytically. A detailed derivation of the first-order partial derivatives $\frac{\partial r}{\partial c}$ and $\frac{\partial c}{\partial x_n}$ is presented in Appendix C, as gradient information is essential for the trust-region-reflective algorithm.

The implementation of the optimisation problem described in Eq. (30) is depicted in Algorithm 2. Here, the first-order partial derivative $\frac{\partial R}{\partial x_n}$ is utilised to minimise the residual R with respect to the stiffness D and A_{44} using the trust-region-reflective algorithm. In practice, the optimisation is executed using the "fmincon" function in Matlab. Termination conditions include reaching the maximum number of iterations ('MaxIterations'), ensuring the change in design variables is below the 'StepTolerance', and ensuring the reduction in the objective residual is below the 'FunctionTolerance'.

2.7. Triangulation: Impact localisation based on the optimised WVP

Once the WVP $c(\theta;\, D_{\text{opt}}, A_{44}^{\text{opt}}, \omega_{\text{opt}})$ of the impact-induced flexural waves has been optimised based on training impacts, the location of the target impact can be estimated using the triangulation method, which involves minimising the difference between the estimated TDOA from the optimised WVP and the extracted TDOA from sensor signals. This optimisation problem for impact localisation is expressed as:

$$\begin{aligned} &x, y = \arg\min_{x,y} R = \arg\min_{x,y} \sum_{j=2}^{N_s} r^2, \\ &r = t_j - t_1 - \Delta t_{1j} = \frac{d_j}{c(\theta_j)} - \frac{d_1}{c(\theta_1)} - \Delta t_{1j}, \\ &d_j = \sqrt{(x - x_j)^2 + (y - y_j)^2}, j = 1, 2, \ldots, N_s, \\ &\theta_j = \arccos \frac{x_j - x}{d_j}, j = 1, 2, \ldots, N_s, \end{aligned} \tag{32}$$

where (x, y) represent the location coordinates of the target impact, (x_j, y_j) denotes the location coordinates of the jth sensor, d_j indicates the distance between the target impact and the jth sensor, θ_j is the direction from the target impact location to the jth sensor, and $c(\theta_j)$ is the optimised wave velocity in the θ_j direction.

To avoid the use of the time-consuming GA algorithm, the trust-region-reflective algorithm is employed to address this optimisation problem efficiently. The first and second-order derivatives $\frac{\partial R}{\partial x}$, $\frac{\partial R}{\partial y}$, $\frac{\partial^2 R}{\partial x^2}$, $\frac{\partial^2 R}{\partial y^2}$, $\frac{\partial^2 R}{\partial x \partial y}$ of the objective residual R with respect to the impact location coordinates x and y are derived using the chain rule:

$$\begin{aligned} &\frac{\partial R}{\partial x} = \sum_{j=2}^{N_s} 2r \frac{\partial r}{\partial x}, \ \frac{\partial R}{\partial y} = \sum_{j=2}^{N_s} 2r \frac{\partial r}{\partial y}, \\ &\frac{\partial^2 R}{\partial x^2} = \sum_{j=2}^{N_s} 2(\frac{\partial r}{\partial x})^2 + 2r \frac{\partial^2 r}{\partial x^2}, \\ &\frac{\partial^2 R}{\partial y^2} = \sum_{j=2}^{N_s} 2(\frac{\partial r}{\partial y})^2 + 2r \frac{\partial^2 r}{\partial y^2}, \\ &\frac{\partial^2 R}{\partial x \partial y} = \sum_{j=2}^{N_s} 2 \frac{\partial r}{\partial x} \frac{\partial r}{\partial y} + 2r \frac{\partial^2 r}{\partial x \partial y}. \end{aligned} \tag{33}$$

These intermediate partial derivatives $\frac{\partial r}{\partial x}$, $\frac{\partial r}{\partial y}$, $\frac{\partial^2 r}{\partial x^2}$, $\frac{\partial^2 r}{\partial y^2}$, $\frac{\partial^2 r}{\partial x \partial y}$ can be derived using the chain rule in conjunction with the dispersion equation Eq. (6) and the optimised parameters D_{opt}, A_{44}^{opt}, ω_{opt}. The detailed derivations of these derivatives are provided in Appendix D. Based on this derivative information, Algorithm 3 illustrates the implementation of impact localisation using the triangulation method and the trust-region-reflective algorithm based on the optimised WVP.

The initial impact location in this optimisation can be estimated from the TDOA data. By analysing the TDOA values, the sensor closest to the impact, indicated by the minimum TOA, and the sensor farthest from the impact, indicated by the maximum TOA, can be identified. This information offers a reasonable estimate of the impact location. To enhance the robustness of the localisation process, two initial impact

locations are generated in this study. One is positioned inside the sensor network between the closest and farthest sensors, while the other is situated outside the sensor network near the nearest sensor.

Additionally, the uncertainty of the estimated impact location (x, y) can be quantified based on the triangulation method. For every pair of sensors, such as sensor i and sensor j, where $j > i$, there exists at least one location solution (x_{ji}, y_{ji}) that satisfies the condition for the estimated TDOA $\Delta\hat{t}_{ji} = t_j - t_i = d_j/c(\theta_j) - d_i/c(\theta_i)$ to match the actual TDOA Δt_{ji}.

$$\begin{aligned} t_j - t_1 - \Delta t_{j1} &= \frac{d_j}{c(\theta_j)} - \frac{d_i}{c(\theta_i)} - \Delta t_{ji} \\ &= \frac{\sqrt{(x_{ji}-x_j)^2+(y_{ji}-y_j)^2}}{c(\theta_j)} - \frac{\sqrt{(x_{ji}-x_i)^2+(y_{ji}-y_i)^2}}{c(\theta_i)} - \Delta t_{ji} \\ &= 0. \end{aligned} \tag{34}$$

The solution of the equation above, closest to the estimated impact location (x, y), indicates how the estimated impact location should adjust to nullify the TDOA difference $(\Delta\hat{t}_{ji} = \Delta t_{ji})$. Every pair of sensors (varying i and j) provides a location (x_{ji}, y_{ji}) bounding the estimated impact location (x, y) that satisfies $\Delta\hat{t}_{ji} = \Delta t_{ji}$. The uncertainty (standard deviation) of the estimated impact location can be defined as the average distance between the estimated impact location (x, y) and the bounding locations (x_{ji}, y_{ji}).

$$\sigma_{xy} = \frac{2}{N_s(N_s-1)} \sum_{i=1}^{N_s-1} \sum_{j=i+1}^{N_s} \sqrt{(x_{ji}-x)^2 + (y_{ji}-y)^2}. \tag{35}$$

2.8. TDOA extraction from sensor signals

From the physical relationship described in Eq. (22), careful attention must be given to TDOA extraction to ensure accurate impact localisation. As previously discussed, dispersive flexural waves dominate the impact sensor signals, wherein their higher frequency components propagate faster than their lower frequency counterparts. To precisely determine impact locations, TDOA extraction should consistently rely on identical frequency components across all impacts. However, variations in impact scenarios, such as changes in impact mass or velocity, alter the impact force and result in distinct distributions of frequency components in the sensor signals. Furthermore, the presence of in-plane extensional waves, captured by sensors near the impact point, can affect TDOA extraction. Therefore, a reliable TDOA extraction method is essential for impact localisation, one that can consistently extract TDOA across diverse impact scenarios while disregarding the effects of extensional waves when impacts occur near sensors.

In this study, two widely used envelope-based TDOA extraction methods are considered: Envelope Threshold (ET) [45,47,63] and Normalised Smooth Envelope Threshold (NSET) [48,62]. These methods identify TDOA by determining the earliest time at which the signal envelope crosses a predefined threshold. While the ET method computes envelopes using the Hilbert transform, the NSET method employs Butterworth filtering to calculate the envelopes.

Fig. 2 illustrates the impact signals recorded by four PZT sensors on a composite laminate flat panel and TDOA extraction using ET and NSET methods for this impact. Further details regarding the experimental setup, the impact, and the panel can be found in Section 3, with this impact corresponding to impact number 1 shown in Fig. 4(a). These four PZT sensors, arranged in ascending order of the impact-to-sensor distance, are indexed as [1, 4, 2, 3]. Thus, it is anticipated that the impact-induced wave reaches sensor 1 first and sensor 3 last, resulting in $\Delta t_{j1} > 0, j = 2, 3, 4$ and Δt_{31} attaining maximal values.

From the sensor signals shown in Fig. 2(a) and (b) over two time windows (4 ms and 0.4 ms), initial peaks are observed at a signal amplitude level of 1 V. These peaks indicate the arrival time of impact-induced waves at the sensors, which is crucial for TDOA estimation. However, it is noticeable that the ET method, relying on the Hilbert transform, results in an early rising envelope, as illustrated in Fig. 2(c). These envelopes fail to capture the information of the initial peaks, rendering the extracted TDOA values unreliable. Moreover, considering the varying frequency components in signals for different impact scenarios, the ET method struggles to extract TDOA from the same frequency due to the envelope from the Hilbert transform encompassing all frequency components.

The NSET, on the other hand, offers more flexible frequency control, as the frequency components of the envelope obtained from the low-pass Butterworth filter can be adjusted by the filter's cut-off frequency f_{NSET}. This cut-off frequency f_{NSET} can be roughly selected based on the presence of initial peaks in the envelopes as it increases from a small value, such as 2 kHz. As depicted in Fig. 2(d), when $f_{NSET} = 20$ kHz, the initial peaks are clearly visible in the envelopes for all four sensors, facilitating TDOA extraction through thresholding. Furthermore, the initial peaks of the envelopes accurately represent the wave arrival order and the impact-to-sensor distance, consistent with the previous analysis of $\Delta t_{j1} > 0, j = 2, 3, 4$. Thus, $f_{NSET} = 20$ kHz appears to be a suitable cut-off frequency for TDOA extraction in this flat panel scenario. More details about the implementation procedures of the NSET method can be found in [48,62].

Moreover, it is important to note that the low-pass filter cannot entirely eliminate frequencies above the cut-off frequency [10]. TDOA extraction typically relies on higher frequency components in the signals that exceed the cut-off frequency f_{NSET}. Therefore, it is suggested that this cut-off frequency f_{NSET} can serve as an initial estimate and lower bound for the frequency in the two-stage optimisation of the WVP, as depicted in Algorithm 1. This approach enhances the efficiency of the WVP optimisation process.

3. Experimental setup

To validate the proposed hybrid physics-based and data-driven impact localisation method, experimental impact tests were conducted on a sensorised composite laminate flat panel and a sensorised stringer-stiffened panel. The experimental setup for these impact tests is depicted in Fig. 3. Both the flat panel and stiffened panel used were quasi-isotropic carbon fibre-reinforced laminates (M21/T800s). The stacking sequence of the flat panel was $[0/+45/45/90]_{2s}$, with each ply having a thickness of 0.25 mm. Conversely, the stringer-stiffened panel had a stacking sequence of $[-45/45/0/0/90/0]_s$ for both the single plate region without a stringer and the stringer, with a ply thickness of 0.125 mm. The material properties of a unidirectional lamina are provided in Table 1, essential for the analytical calculation of the wave propagation velocity profile.

The flat panel (290 mm × 200 mm) was equipped with 4 PZT sensors bonded to the top side of the plate (impact side), while the stiffened plate (475 mm × 250 mm) had 4 PZT sensors bonded to the bottom side of the plate to simulate potential sensor installation on the inside of a stiffened aircraft structure. The coverage area of these 4 PZT sensors, both for the flat panels and the stiffened panels, formed a rectangular area.

Impacts were induced by dropping a 20 mm diameter round steel head impactor perpendicular to the panels along the guide rails, as illustrated in Fig. 3(a) and (b). The impactor had a mass of 100 g and was dropped from a height of 20 mm. The layout of the impact locations and sensor positions is depicted in Fig. 4 for both the flat and stiffened panels. A total of 35 drop mass impacts, numbered from 1 to 35, were applied to the composite laminate flat panel, evenly distributed on a 20 × 20 mm grid and all within the sensor network. Conversely, 25 drop mass impacts, numbered 1 to 25, were conducted on the composite laminate stringer stiffened panel. Impacts numbered 1 to 5 and 21 to 25 were slightly outside the sensor network. Additionally, these impacts on the stringer stiffened panel were categorised into three groups based on impact location: 10 impacts on the single panel region without a stringer (numbered 1:5:21, 5:5:25), 10 impacts on the stringer toes (numbered 2:5:22, 4:5:24), and 5 impacts on the panel region between the stringer toes (numbered 3:5:23).

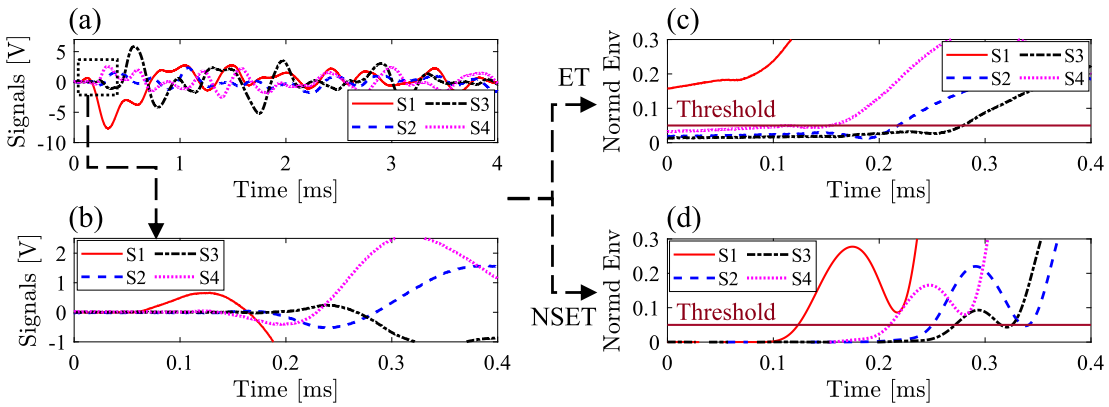


Fig. 2. The TDOA extraction from sensor signals using ET and NSET methods. (a) Impact sensor signals captured by 4 PZT sensors within a time window of 4 ms on a laminated composite flat panel. The highest signal amplitudes occur within the initial time window of 1 ms, after which the signal amplitudes decrease due to structural damping. (b) Sensor signals within the initial 0.4 ms time window. Initial peaks are observed at a signal amplitude level of 1 V, which are crucial for TDOA estimation. (c) The envelopes obtained by the ET method. ET method, relying on the Hilbert transform, results in an early rising envelope. (d) The envelopes obtained by the NSET method. An appropriate cut-off frequency can be determined to retain the initial peaks of the sensor signals in the envelopes.

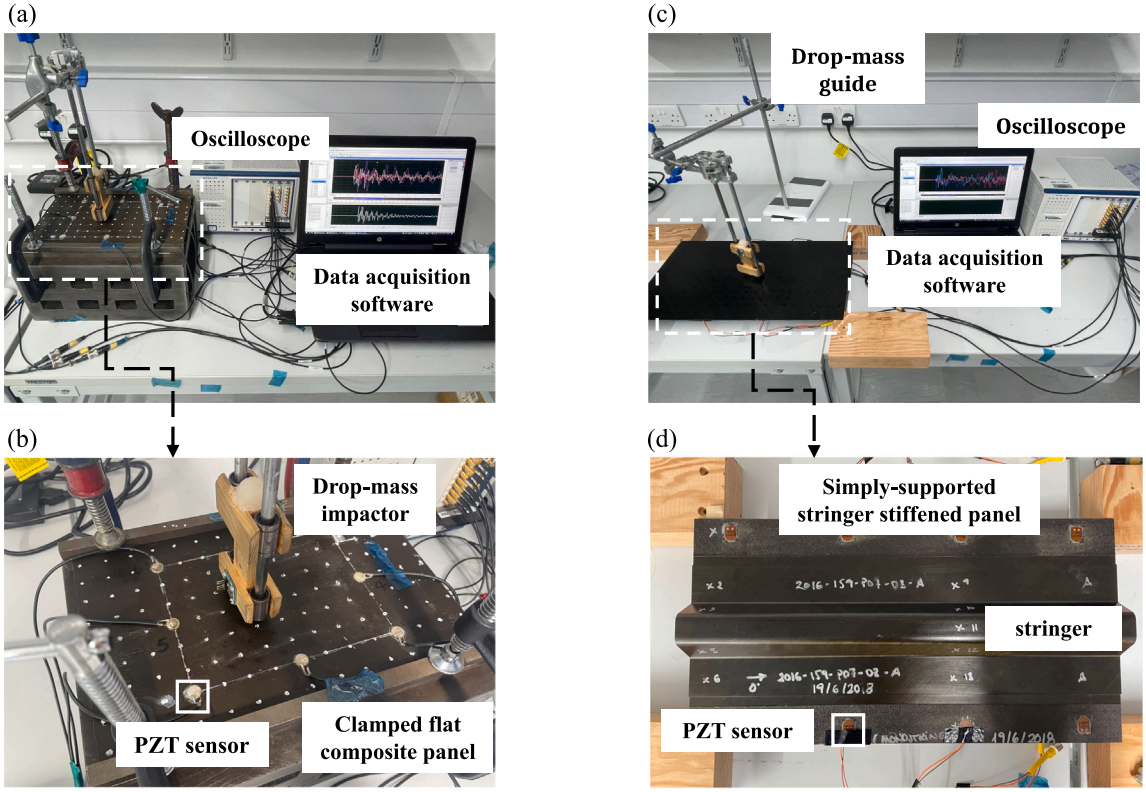


Fig. 3. Experimental setup for impact testing. (a) Impact testing setup of the composite laminate flat panel, utilising a drop mass to generate impacts along a guide rail. (b) The composite laminate flat panel, clamped along its longitudinal edges while the transverse edges remain free. (c) Impact testing setup of the composite laminate stringer-stiffened panel, employing the same drop mass to induce impacts along a guide rail. (d) The stringer stiffened panel, supported simply on the four corners of the panel.

An NI PXI-5105 8-channel oscilloscope and NI SignalExpress software were utilised for sensor signal acquisition. Each PZT sensor was connected to an individual channel of the oscilloscope. The sampling frequency for recording the impact sensor signals was set at 200 kHz, with a fixed sampling window of 50 ms. Each impact was repeated twice for consistency. A total of 70 impact sensor signals were collected from the flat panel, while 50 were collected from the stringer-stiffened panel. Details of these impact tests are summarised in Table 2, where "FP" and "SP" represent the flat and stiffened panels, respectively.

Table 2
Impact tests conducted.

Impact case	Impact machine	Parameters	Number of impacts
FP	Drop mass	m = 100 g, h = 20 mm	70 (loc 1-35 × 2 rpt)
SP	Drop mass	m = 100 g, h = 20 mm	50 (loc 1-25 × 2 rpt)

*m: impact mass, h: impact height, loc: location, rpt: repetitions.

It is important to highlight that the dispersion relations governing the wave profile are derived analytically for simple plates, based on the FSDT. A recent study by Correas [70] presented an analytical impact spring model for predicting impact behaviours of stringer-stiffened composite laminates, utilising the FSDT. In this model, the global stiffness of the stiffened panel is represented by combining the stiffness of its flat plate component and the stringer component. Validation of this analytical impact spring modelling was conducted using FEM

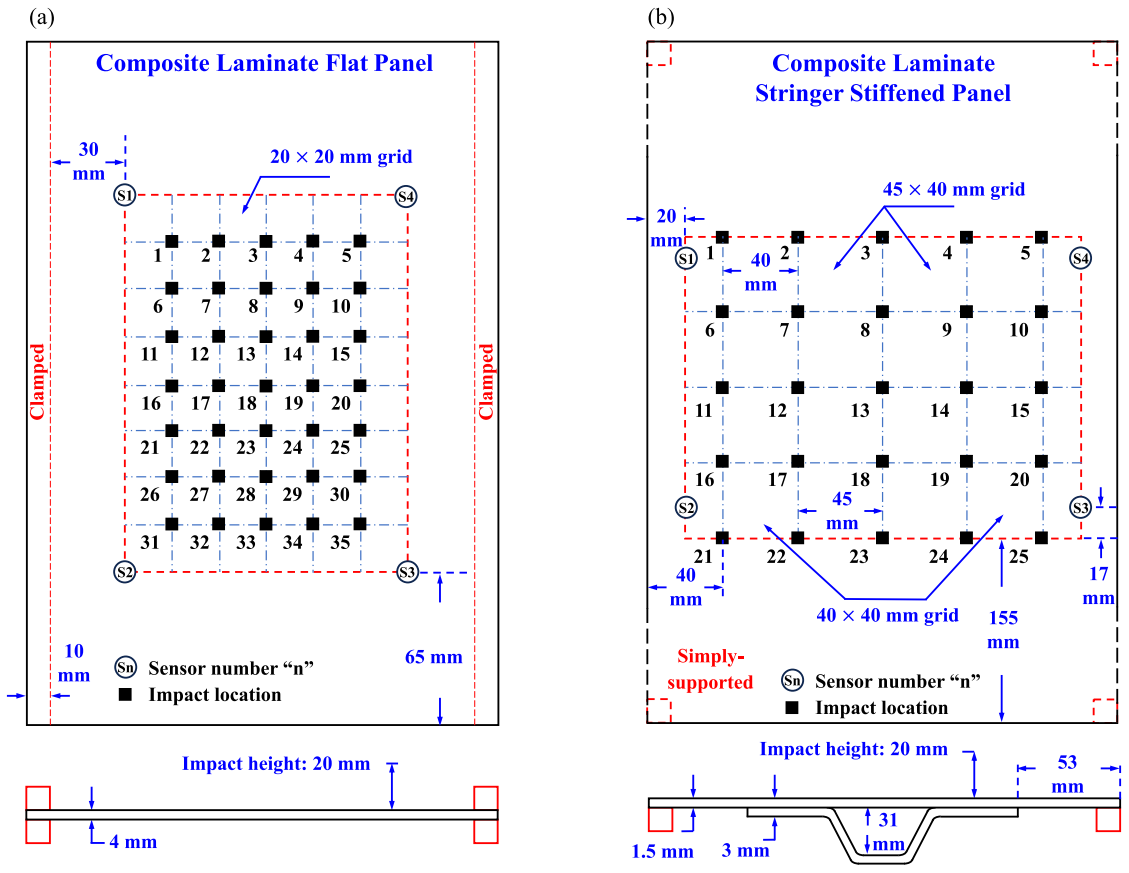


Fig. 4. Layout of composite laminate flat and stiffened panels. (a) The flat panel, measuring 290 mm × 200 mm, was equipped with 4 PZT sensors bonded to the top side of the plate (impact side). A total of 35 impact locations, numbered 1–35, are uniformly distributed inside the sensor network. (b) The stringer-stiffened panel, measuring 475 mm × 250 mm, had 4 PZT sensors bonded to the bottom side of the plate (opposite to the impact). A total of 25 impact locations are designated on this panel, with impacts numbered 1–5 and 21–25 slightly outside of the sensor network.

models, which demonstrated a close estimation of the impact force history.

Building upon this work, stringer-stiffened composite laminates can be effectively approximated by a simplified plate model, where the equations of motion of simple plates approximately govern the motions of the stringer-stiffened composite laminates using the global stiffness. In other words, the dispersion relations derived from the equations of motion of simple plates can also be used to parameterise the WVP of the stringer-stiffened composite laminates. The purpose of conducting impact tests on the stringer-stiffened panel is to validate the effectiveness of the proposed hybrid impact localisation method on more complex stiffened structures. This validation is essential, considering that the majority of aircraft structures are intricate and incorporate stiffening elements.

4. The optimisation of wave velocity profile

The experimental impact data were utilised to validate the proposed hybrid physics-based and data-driven impact localisation method, which optimises the WVP using a two-stage approach based on training impacts and locates the target impact through triangulation based on the optimised WVP. For the composite laminate flat panel, four experimental impacts numbered 12, 14, 22, and 24, as shown in Fig. 4(a), were utilised as the training impacts. Similarly, the same number of training impacts, numbered 7, 9, 17, and 19 and displayed in Fig. 4(b), were adopted for the stringer-stiffened panel. Subsequently, all experimental impacts were treated as testing impacts (target impacts) based on the optimised WVP, aiming to be localised by minimising the difference in TDOA between the optimised WVP and sensor signals.

The accuracy of the WVP and impact localisation hinges on factors such as the optimisation algorithm, the number of sensors employed, and the quantity of training impacts. In this section, the number of sensors was fixed at four, which is a reasonable choice, as in practical scenarios, the aircraft structure can be segmented into numerous substructures using the closest four sensors. Additionally, the effects of the number of sensors were investigated on impact localisation Section 5.3.

With the aforementioned four training impacts, the proposed two-stage approach was compared with the GA for optimising the WVP as described in Eq. (23). The stiffness design variables $D_{ij}, i, j = 1, 2, 6$, and A_{44} are determined using the laminate properties detailed in Table 1 and the stacking sequence. A scaling range of $[0.8, 1.2]$ is employed to accommodate stiffness uncertainties in the optimisation. For the frequency ω, the cut-off frequency f_{NSET} utilised in TDOA extraction via the NSET method serves as its nominal value, with the frequency bounded empirically within $[1, 30]f_{NSET}$ during optimisation.

In addition, the GA algorithm utilises an initial population size of 100, determined through Latin hypercube sampling in the eight-dimensional design space, with each iteration employing the same population size. Conversely, the proposed two-stage approach necessitates an initial point defined by the nominal values of the optimisation design variables.

The convergence of the objective residual, to be minimised during the velocity profile optimisation, is illustrated in Fig. 5 for both the flat and stiffened panels. In the figure legend, "TS" denotes the proposed two-stage approach.

It is evident that the proposed two-stage approach achieves convergence much more rapidly compared to the GA algorithm for both flat and stiffened panels. The proposed method requires fewer than 40 objective residual evaluations in total to minimise the objective

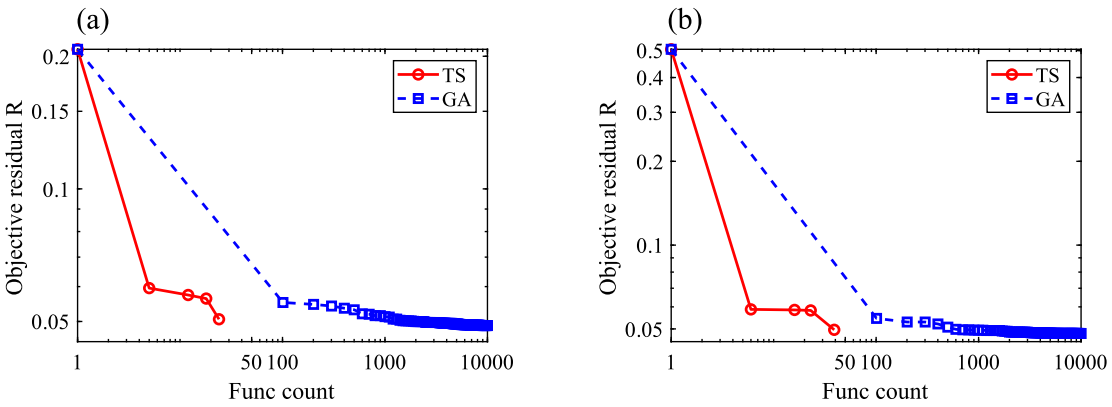


Fig. 5. Convergence of objective residual for WVP optimisation: (a) flat panel (FP), (b) stringer stiffened panel (SP). For both panels, the proposed two-stage (TS) method requires fewer than 40 objective residual evaluations in total to minimise the objective residual to a value that would typically necessitate 1000 objective residual evaluations with GA.

Table 3
Computational time for the velocity profile optimisation.

Algorithm	Computational time (FP)	Computational time (SP)
TS	2.24 s	3.59 s
GA (1000 FC)	18.95 s	26.55 s
GA (10000 FC)	179.13 s	242.59 s

*FC: function counts.

residual to a value that would typically necessitate 1000 objective residual evaluations with GA. In the first stage, which optimises the WVP with respect to the frequency using Newton's method, convergence is achieved in less than 5 iterations, with fewer than 5 objective residual evaluations in each iteration. Subsequently, the second stage, which optimises the WVP with respect to stiffness, further reduces the objective residual significantly in a single large step. In contrast, the GA algorithm's initial population yields a relatively small value of the objective residual, with subsequent iterations exploring the design space at a higher computational cost, resulting in limited improvement.

Table 3 presents the average computational time of 10 repetitions for both the two-stage approach and GA to optimise the WVP on an Intel i7-10700 processor. The proposed two-stage approach demonstrates nearly an 8-fold improvement in speed compared to GA for WVP optimisation. It takes less than 4 seconds for the proposed two-stage approach to identify the optimised WVP.

The optimised WVP for both the flat and stiffened panels, obtained through the proposed two-stage approach and GA, are depicted in Fig. 6. The label "FS" in the figures denotes the first-stage, representing the WVP optimised with respect to frequency. It is noteworthy that the first-stage optimised velocity profile (FS) closely approximates the final optimised results of the two-stage approach (TS) and GA. This observation underscores the significance of frequency as the primary design variable influencing wave velocity amplitude. Furthermore, the optimised WVP obtained through the two-stage approach (TS) and GA exhibit remarkable similarity, underscoring the effectiveness of the proposed two-stage approach for efficient WVP optimisation.

5. Impact localisation on the experimental flat and stiffened panels

With the optimised WVP obtained through the proposed two-stage approach, the impact locations and localisation uncertainties for the target impacts can be identified via triangulation. This process involves utilising the trust-region-reflective algorithm to solve another optimisation problem, as depicted in Algorithm 3. This hybrid physics-based and data-driven impact localisation method is denoted as HPD.

As a reference method, the widely used data-driven impact localisation method employing ANN is adopted. The ANN architecture aligns with previous research [47], which demonstrated that a configuration comprising 4 layers, each with 10 neurons utilising hyperbolic tangent sigmoid function as activation, and Fletcher-Powell conjugate gradient as the training function, yielded satisfactory localisation accuracy for large-scale stiffened panels. The number of training epochs for the ANN is set to 50000, with a learning rate of 0.01. The ANN training process is repeated 200 times to address model uncertainty. The final location estimation of the target impacts is obtained as the average location prediction from these 200 repetitions, while the localisation uncertainty is quantified by the standard deviation of these 200 predictions.

The structure of this section is organised as follows: the subsequent two subsections present the results of impact localisation by HPD and ANN on the experimental flat panel and the stiffened panel, respectively. Additionally, the final subsection investigates the effects of the number of sensors employed on impact localisation.

5.1. Impact localisation on the flat panel

As previously stated, for the composite laminate flat panel, four experimental impacts numbered 12, 14, 22, and 24, as shown in Fig. 4(a), were utilised as the training impacts. The target impacts (testing impacts) to be localised encompassed all 35 experimental impacts, some of which were situated outside the coverage area of the four training impacts. The localisation outcomes of the proposed HPD and ANN are depicted in Fig. 7, where solid red circles represent the sensors, hollow black diamonds denote the training impacts, solid blue squares represent the target impacts, solid magenta hexagons indicate the identified locations of the target impacts, and the dashed magenta ellipses represent the uncertainties (standard deviations) of the identified locations. The uncertainties of the locations estimated by the ANN method are not plotted in the figure because they are so large that including them would distort the presentation of the localisation results.

With only four training impacts, the proposed HPD method accurately localises the target impacts regardless of whether they are within or outside the training impact coverage area. In contrast, the ANN method fails to localise impacts outside the training impact coverage area because it relies solely on training impact data without incorporating any physical information. The accuracy of the ANN extrapolation cannot be guaranteed, and its predictions typically tend to closely resemble the training data.

However, the proposed HPD method explicitly derives the WVP through optimisation, which is the exact physics model that the ANN aims to approximate. By integrating physics information with training impact data, the proposed HPD method can effectively locate impacts outside the training impact coverage area. Moreover, the incorporation of physics information also reduces the training impact requirements. The effectiveness of the proposed method is demonstrated by its ability to accurately localise impacts based on only four training impacts.

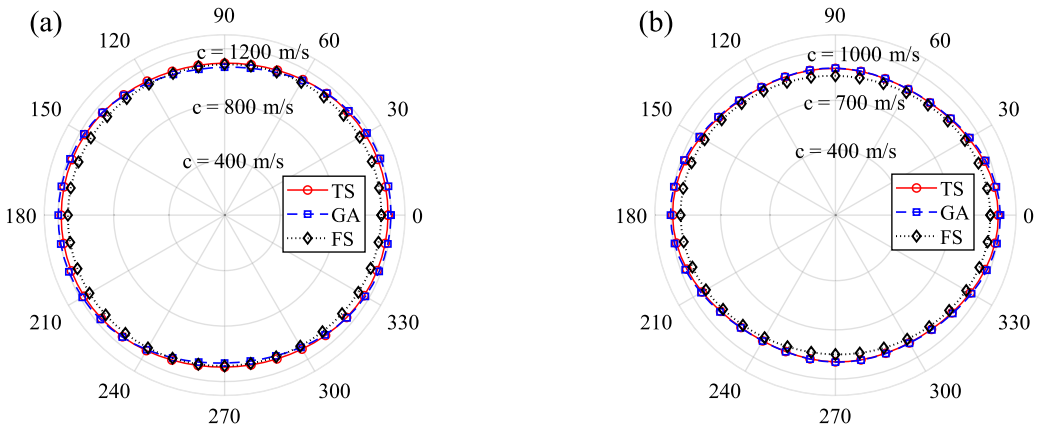


Fig. 6. The optimised WVP based on four training impacts: (a) flat panel (FP), (b) stringer stiffened panel (SP). For both panels, the proposed two-stage (TS) method optimised the WVP to an extent almost identical to the time-consuming GA. Particularly, the first-stage (FS) optimised WVP closely approximates the final optimised results, indicating the significance of the wave frequency for controlling the wave velocity amplitude.

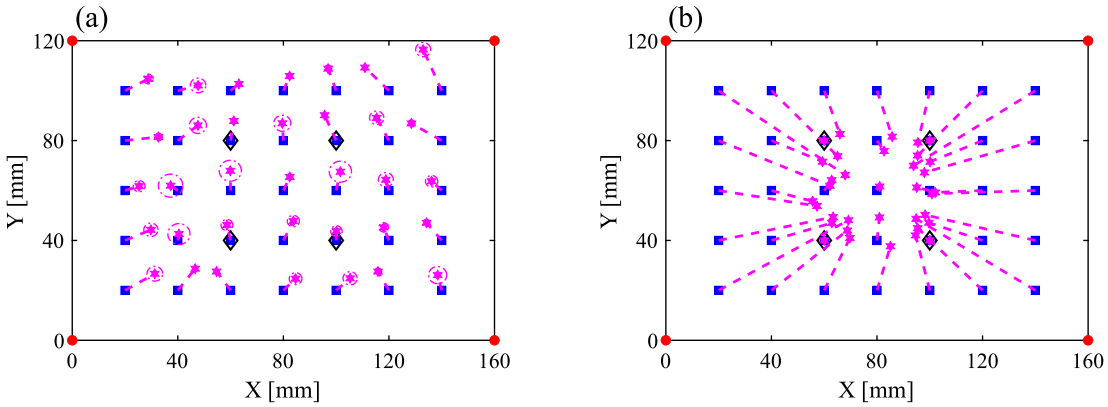


Fig. 7. Impact localisation of the flat panel. (a) The proposed HPD method accurately located impacts outside the coverage area of the four training impacts with high localisation confidence. (b) ANN failed to locate impacts outside the training coverage area due to its exploration limitations.

Table 4
Impact localisation results of the flat panel.

Localisation method	Mean error [mm]	Max error [mm]	Mean SD [mm]	Max SD [mm]
HPD	8.27	17.89	2.15	4.62
ANN	25.67	56.39	11.36	17.52

Table 4 presents a summary of the impact localisation outcomes for the flat panel using both the HPD and ANN methods. The mean error and maximum error in the table represent the average and maximum localisation errors, respectively, across the 35 target impacts. Additionally, the average and maximum standard deviations (SD) indicate the uncertainties associated with these impacts.

Comparing the two methods, the proposed HPD method exhibits higher accuracy, as evidenced by its smaller mean and maximum localisation errors, as well as more reliable location estimation, indicated by its smaller mean and maximum standard deviations, in contrast to the ANN method. Specifically, the HPD method yields a mean localisation error of 8.27 mm and a mean standard deviation of 2.15 mm, while the corresponding values for the ANN method are 25.67 mm and 11.36 mm, respectively.

5.2. Impact localisation on the stringer stiffened panel

To validate the proposed HPD impact localisation method on stiffened composite structures, impact tests were conducted on a composite laminate stringer-stiffened panel, as illustrated in Figs. 3 and 4. The experimental impacts numbered 7, 9, 17, and 19 were utilised as training impacts to optimise the velocity profile. Subsequently, all 25 impacts were employed as target impacts to assess the localisation accuracy of the proposed HPD method.

Fig. 8 presents a comparison of impact localisation between the proposed HPD method and ANN on the stiffened panel, based on the four selected training impacts. The markers in this figure have the same representation as those in the flat panel depiction shown in Fig. 7. The results demonstrate that, similar to the flat panel, the proposed HPD method accurately locates the target impacts, regardless of whether they fall within or outside the training impact coverage area. In contrast, ANN fails to localise impacts beyond the training impact coverage area. Additionally, impacts numbered 1–5 and 21–25, located slightly outside the sensor network, are successfully localised by the proposed HPD method.

The localisation errors and uncertainties are summarised in Table 5. Similar to the flat panel results, the proposed HPD method offers more accurate and reliable impact location estimation, as indicated by smaller localisation errors and standard deviations compared to ANN. Specifically, the proposed HPD method achieves a mean localisation error of 12.65 mm and a mean standard deviation of 8.91 mm, whereas ANN exhibits corresponding values of 36.38 mm and 20.13 mm, respectively.

The precise impact localisation achieved by the proposed HPD method on the stringer-stiffened panel validates its applicability to stiffened composite laminate structures. This applicability arises from the fact that stiffened composite laminate panels can be effectively approximated by simple plates with global stiffness [70]. Additionally, the proposed HPD method demonstrates robustness to variations in

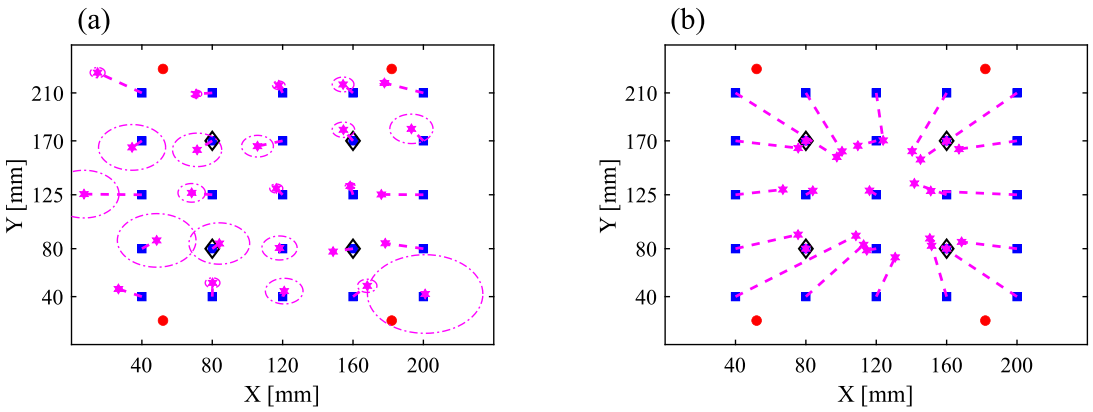


Fig. 8. Impact localisation of the stiffened panel. (a) The proposed HPD method accurately located impacts outside the training coverage area and even outside the sensor network. The accurate impact localisation on the stiffened panel underscores the potential application of the proposed HPD method to real-world composite stiffened aircraft structures. (b) ANN failed to locate impacts outside the training coverage area due to its exploration limitations.

Table 5
Impact localisation results of the stiffened panel.

Localisation method	Mean error [mm]	Max error [mm]	Mean SD [mm]	Max SD [mm]
HPD	12.65	32.90	8.91	32.81
ANN	36.38	89.28	20.13	40.31

Table 6
Impact localisation results of the flat panel with three and four sensors.

Case	Sensor	Mean error [mm]	Max error [mm]
Comb1	1, 2, 3	9.90	21.21
Comb2	1, 2, 4	9.01	15.58
Comb3	1, 3, 4	10.71	20.20
Comb4	2, 3, 4	10.00	23.60
All	1, 2, 3, 4	8.27	17.89

structural stiffness since the WVP for locating impacts is optimised with respect to wave frequency and stiffness through a two-stage approach based on training impact data. In this optimisation process, the amplitude of the WVP is primarily controlled by the wave frequency, while the shape of the WVP is fine-tuned by variations in material stiffness.

This analysis suggests that the HPD method is suitable for locating impacts on real aircraft composite laminate stiffened structures. Moreover, leveraging physical information from laminate properties and stacking sequences significantly reduces the training data requirements. With just four training impacts, impacts can be located with a localisation error of approximately 10 mm and a standard deviation of 10 mm for both flat and stringer-stiffened panels.

5.3. The effects of number of sensors on the impact localisation

Although studies on sensor placement optimisation have demonstrated that optimal impact identification performance is achieved when the sensors are positioned at the corners of the plate, maximising the coverage area [71–73], it is worthwhile to investigate the effects of the number of sensors on impact localisation using the proposed HPD method. It is well established that at least 3 sensors are required for the triangulation method to determine a unique impact location [28]. The proposed HPD impact localisation method can also operate effectively with three sensors. Fig. 9 illustrates the impact localisation of the flat panel using four combinations of three sensors (four sensors form 4 combinations of three sensors). It is evident that impacts are accurately located for all four sensor combinations.

Table 6 presents statistics on the localisation accuracy of the flat panel using three and four sensors. The mean localisation errors for the four combinations of three sensors range from 9 to 11 mm, while the maximum localisation errors range from 15.58 to 23.60 mm. Increasing the number of sensors from 3 to 4 enhances the overall localisation accuracy, with the mean localisation error decreasing to 8.27 mm, and the maximum localisation error falls within the range observed for three sensors.

Additionally, increasing the number of sensors improves the reliability and robustness of the impact localisation system, particularly in accounting for sensor malfunctions. While the effectiveness of the proposed HPD with three sensors is validated for impact localisation, including more sensors is preferable for ensuring reliability and accuracy. This is also true in real-world applications, where large-scale structures are typically equipped with at least tens of sensors.

6. Conclusions

A novel hybrid physics-based and data-driven impact localisation method was developed in this study for composite laminates, termed the HPD method, integrating the physical dispersion relations of impact-induced flexural waves into the localisation process. The dispersion relations of flexural waves, derived from FSDT, parameterise the WVP with respect to material stiffness and wave frequency. A two-stage approach was developed for the optimisation of WVP based on training impacts, utilising solely gradient-based optimisation algorithms. This optimised WVP was subsequently employed for impact localisation by the triangulation method.

Experimental validation of the proposed HPD method involves conducting impact testing on a composite laminate flat panel and stringer-stiffened panel using drop mass. The results demonstrate that the HPD method accurately localises impacts with just four training impacts, even when impacts occur outside the training impact coverage area, a capability not matched by ANN. The successful application of the HPD method to the composite laminate stringer-stiffened panel underscores its potential for localising impact events in real-world composite stiffened aircraft structures.

Moving forward, future research directions include the development of a probabilistic framework for impact localisation based on the proposed HPD method, which accounts for uncertainties arising from the training impact data. Additionally, refining a TDOA extraction method to accurately and consistently estimate TDOA across various impact scenarios is crucial for generalising the proposed HPD method to a wide range of impact situations. Moreover, aiming for accurate and reliable impact identification with a small number of training impacts necessitates the development of a physics-based and data-driven method for precise and robust impact force reconstruction. These research endeavors form the foundation for analysing impact damages and monitoring structural health.

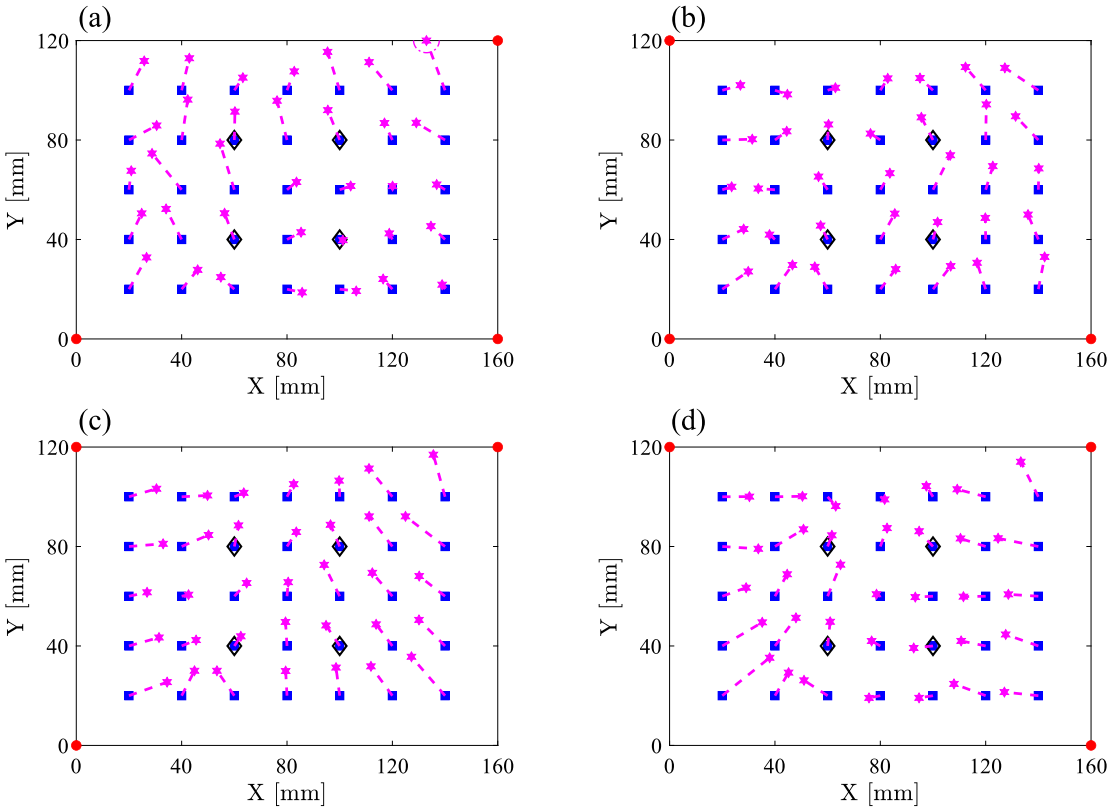


Fig. 9. Impact localisation of the flat panel with three sensors. (a) Sensor combination 1 (sensors numbered 1, 2, 3). (b) Sensor combination 2 (sensors numbered 1, 2, 4). (c) Sensor combination 3 (sensors numbered 1, 3, 4). (d) Sensor combination 4 (sensors numbered 2, 3, 4). For all four sensor combinations, impacts are quite accurately located.

CRediT authorship contribution statement

Dong Xiao: Writing – review & editing, Writing – original draft, Software, Methodology, Conceptualization. **Zahra Sharif-Khodaei:** Writing – review & editing, Supervision, Methodology, Conceptualization. **M.H. Aliabadi:** Writing – review & editing, Supervision, Methodology, Conceptualization.

Declaration of competing interest

The authors declare that they have no known competing financial interests or personal relationships that could have appeared to influence the work reported in this paper.

Data availability

Data will be made available on request.

Acknowledgements

The first author would like to acknowledge and express gratitude to the China Scholarship Council for providing a scholarship to fund his Ph.D. studies (Scholarship No. [2021]339). Additionally, the authors would like to thank Dr. Francisco de Sá Rodrigues for manufacturing and providing the experimental stiffened panel.

Appendix A. Equations of motion of laminated composite plates based on FSDT

Illustrated in Fig. 10, a rectangular laminated composite plate with a total thickness h consists of four orthotropic layers and is analysed using two commonly employed plate theories: CPT and FSDT. CPT assumes negligible shear strain, shear deformation, and rotational inertia, allowing the mid-surface plane to fully represent the motion of a three-dimensional plate. In contrast, FSDT considers a non-zero constant shear strain along the plate thickness, resulting in a linear displacement variation throughout the thickness.

For a symmetrically laminated plate, the in-plane motion and transverse motion are decoupled. Neglecting body forces, the equations governing in-plane motion in terms of displacements are provided as follows [31,74,75]:

$$\begin{aligned} &A_{11}\frac{\partial^2 u}{\partial x^2}+A_{66}\frac{\partial^2 u}{\partial y^2}+2A_{16}\frac{\partial^2 u}{\partial x\partial y}+A_{16}\frac{\partial^2 v}{\partial x^2}\\ &\quad+A_{26}\frac{\partial^2 v}{\partial y^2}+(A_{12}+A_{66})\frac{\partial^2 v}{\partial x\partial y}=I_1\frac{\partial^2 u}{\partial t^2},\\ &A_{16}\frac{\partial^2 u}{\partial x^2}+A_{26}\frac{\partial^2 u}{\partial y^2}+(A_{12}+A_{66})\frac{\partial^2 u}{\partial x\partial y}\\ &\quad+A_{66}\frac{\partial^2 v}{\partial x^2}+A_{22}\frac{\partial^2 v}{\partial y^2}+2A_{26}\frac{\partial^2 v}{\partial x\partial y}=I_1\frac{\partial^2 v}{\partial t^2}. \end{aligned} \tag{36}$$

The equations governing transverse (out-of-plane) motion are derived as follows:

$$\begin{aligned} &A_{55}(\frac{\partial\psi_x}{\partial x}+\frac{\partial^2 w}{\partial x^2})+A_{45}(\frac{\partial\psi_x}{\partial y}+\frac{\partial\psi_y}{\partial x}+2\frac{\partial^2 w}{\partial x\partial y})\\ &\quad+A_{44}(\frac{\partial\psi_y}{\partial y}+\frac{\partial^2 w}{\partial y^2})=I_1\frac{\partial^2 w}{\partial t^2},\\ &D_{11}\frac{\partial^2\psi_x}{\partial x^2}+D_{66}\frac{\partial^2\psi_x}{\partial y^2}+2D_{16}\frac{\partial^2\psi_x}{\partial x\partial y}+D_{16}\frac{\partial^2\psi_y}{\partial x^2}\\ &\quad+D_{26}\frac{\partial^2\psi_y}{\partial y^2}+(D_{12}+D_{66})\frac{\partial^2\psi_y}{\partial x\partial y}-A_{55}(\psi_x+\frac{\partial w}{\partial x})\\ &\quad-A_{45}(\psi_y+\frac{\partial w}{\partial y})=I_3\frac{\partial^2\psi_x}{\partial t^2},\\ &D_{16}\frac{\partial^2\psi_x}{\partial x^2}+D_{26}\frac{\partial^2\psi_x}{\partial y^2}+(D_{12}+D_{66})\frac{\partial^2\psi_x}{\partial x\partial y}+D_{66}\frac{\partial^2\psi_y}{\partial x^2}\\ &\quad+D_{22}\frac{\partial^2\psi_y}{\partial y^2}+2D_{26}\frac{\partial^2\psi_y}{\partial x\partial y}-A_{45}(\psi_x+\frac{\partial w}{\partial x})\\ &\quad-A_{44}(\psi_y+\frac{\partial w}{\partial y})=I_3\frac{\partial^2\psi_y}{\partial t^2}. \end{aligned} \tag{37}$$

where u, v, w represent the mid-plane displacements in the x, y, z direction respectively, while ψ_x, ψ_y denote the rotations of the normal to the mid-plane about the y and x axes respectively (illustrated in Fig. 10). Additionally, h, ρ represent the plate thickness and density, $I_1 = \rho h$

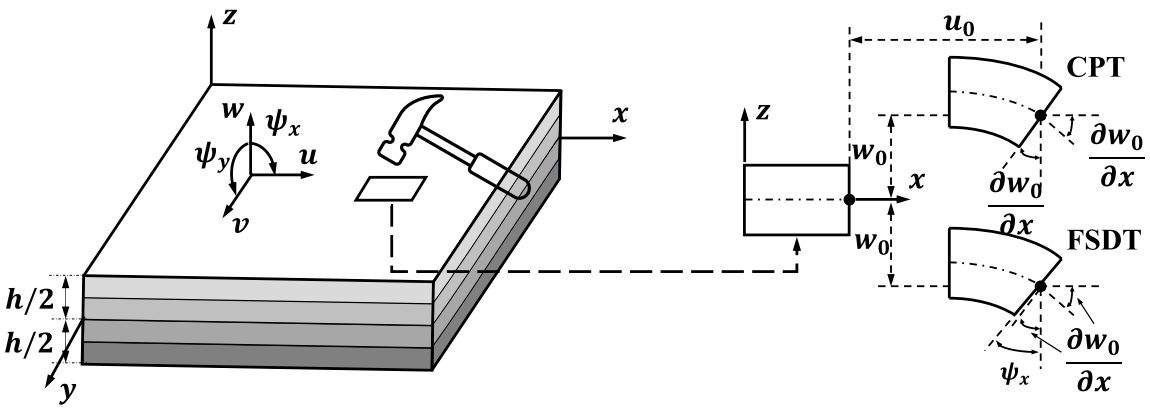


Fig. 10. Laminated composite plate and plate theories (CPT and FSDT). When subjected to impact from a hammer, a rectangular laminated composite plate with a total thickness h, comprising four orthotropic layers, undergoes deformation. The deformations (wave propagation) during impact can be analysed analytically using plate theories, such as CPT or FSDT, each based on its respective assumptions.

denotes the mass per unit length, $I_3 = \int_{-h/2}^{h/2} \rho z^2 dz$ is typically referred to as the rotational inertia. The laminate stiffness is given by:

$$\begin{aligned} &(A_{ij}, D_{ij}) = \int_{-h/2}^{h/2} (\bar{Q}_{ij})_k (1, z^2) dz, i, j = 1, 2, 6, \\ &A_{ij} = \alpha^2 \int_{-h/2}^{h/2} (\bar{Q}_{ij})_k dz, i, j = 4, 5, \end{aligned} \tag{38}$$

where $\bar{Q}_{ij}$ for $i, j = 1, 2, 6$ represent the plane-stress reduced stiffness, $\bar{Q}_{ij}$ for $i, j = 4, 5$ denote the transverse shear stiffness. To account for the non-uniform distribution of shear strain across the plate thickness, a shear correction factor α is introduced. Typically, this factor is taken as $\pi^2/12$ [31].

Appendix B. Dispersion relations of flexural waves based on CPT

Formulated from the CPT, the equation describing the out-of-plane motion of the midplane, neglecting body forces, is derived as a fourth-order partial differential equation [74,76]:

$$\begin{aligned} &D_{11} \frac{\partial^4 w}{\partial x^4} + 2(D_{12} + 2D_{66}) \frac{\partial^4 w}{\partial x^2 y^2} + D_{22} \frac{\partial^4 w}{\partial y^4} \\ &+4D_{16} \frac{\partial^4 w}{\partial x^3 \partial y} + 4D_{26} \frac{\partial^4 w}{\partial x \partial y^3} + I_1 \frac{\partial^2 w}{\partial t^2} = 0. \end{aligned} \tag{39}$$

Assuming the harmonic waveform $w = We^{ik(r-ct)}, r = x\cos\theta + y\sin\theta$ and substituting it into Eq. (39), the dispersion relations of flexural waves based on CPT are derived as follows:

$$\begin{aligned} \frac{I_1 c^4}{\omega^2} &= D_{11}\cos^4\theta + 2(D_{12} + 2D_{66})\sin^2\theta\cos^2\theta \\ &+ D_{22}\sin^4\theta + 4D_{16}\sin\theta\cos^3\theta + 4D_{26}\sin^3\theta\cos\theta. \end{aligned} \tag{40}$$

Clearly, this dispersion equation governs only one wave mode. The flexural waves of this mode exhibit dispersive characteristics, wherein the phase velocity c increases linearly with the square root of the frequency $\sqrt{\omega}$. However, this phase velocity is unbounded and approaches infinity as the wave frequency tends to infinity, which is impractical in reality. In real structures, the rotational inertia, neglected in CPT, serves to limit the phase velocity as the frequency approaches infinity.

Appendix C. The partial derivative of objective residual with respect to stiffness

In the second stage of the optimisation of the WVP, the first-order partial derivatives $\frac{\partial R}{\partial x_n}$ of objective residual R with respect to stiffness variable $x_n \in (D, A_{44})$, as derived in Eq. (31), are expressed with intermediate derivatives $\frac{\partial r}{\partial c}, \frac{\partial c}{\partial x_n}$ using the chain rule. These intermediate derivatives can be straightforwardly obtained based on the expression of r illustrated in Eq. (30):

$$\begin{aligned} &\frac{\partial r}{\partial c} = [-\frac{d_{ij}}{c^2(\theta_{ij};\, D, A_{44}, \omega_{opt})}, \frac{d_{i1}}{c^2(\theta_{i1};\, D, A_{44}, \omega_{opt})}], \\ &\frac{\partial c}{\partial x_n} = [\frac{\partial c(\theta_{ij};\, D, A_{44}, \omega_{opt})}{\partial x_n}, \frac{\partial c(\theta_{i1};\, D, A_{44}, \omega_{opt})}{\partial x_n}]. \end{aligned} \tag{41}$$

The partial derivative $\frac{\partial c}{\partial x_n}$ (representing the derivative of velocity c with respect to the stiffness $x_n \in (D, A_{44})$) is crucial information for the trust-region-reflective algorithm when optimising the WVP with respect to stiffness $x_n \in (D, A_{44})$. Eq. (18) provides a standardised expression for computing this partial derivative, involving intermediate variables $a_{ij}, g_{ij}, i, j = 1, 2, 3$. When the frequency ω is fixed, the first-order partial derivative of $g_{ij}, i, j = 1, 2, 3$ with respect to stiffness $x_n \in (D, A_{44})$ can be derived as:

$$\begin{aligned} &\frac{\partial g_{11}}{\partial x_n} = \frac{\omega^2}{c^2}(\frac{2A_{44}}{c}\frac{\partial c}{\partial x_n} - \frac{\partial A_{44}}{\partial x_n}), \\ &\frac{\partial g_{12}}{\partial x_n} = i\cos\theta\frac{\omega}{c}(\frac{-A_{44}}{c}\frac{\partial c}{\partial x_n} + \frac{\partial A_{44}}{\partial x_n}), \\ &\frac{\partial g_{13}}{\partial x_n} = i\sin\theta\frac{\omega}{c}(\frac{-A_{44}}{c}\frac{\partial c}{\partial x_n} + \frac{\partial A_{44}}{\partial x_n}), \\ &\frac{g_{22}}{\partial x_n} = \frac{\omega^2}{c^2}(\frac{\partial b_{22}}{\partial x_n} - \frac{2b_{22}}{c}\frac{\partial c}{\partial x_n}) + \frac{\partial A_{44}}{\partial x_n}, \\ &\frac{g_{23}}{\partial x_n} = \frac{\omega^2}{c^2}(\frac{\partial b_{23}}{\partial x_n} - \frac{2b_{23}}{c}\frac{\partial c}{\partial x_n}), \\ &\frac{g_{33}}{\partial x_n} = \frac{\omega^2}{c^2}(\frac{\partial b_{33}}{\partial x_n} - \frac{2b_{33}}{c}\frac{\partial c}{\partial x_n}) + \frac{\partial A_{44}}{\partial x_n}, \end{aligned} \tag{42}$$

where the expressions of b_{22}, b_{23}, b_{33} are given in Eq. (10). Substituting Eq. (42) into Eq. (18), $\frac{\partial c}{\partial x_n}$ is derived as follows:

$$\begin{aligned} &\frac{\partial c}{\partial x_n} = \frac{c}{2\omega}\frac{Num_1 + Num_2}{Den}, \\ &Num_1 = \frac{\omega^2}{c^2}(-a_{11}\frac{\partial A_{44}}{\partial x_n} + a_{22}\frac{\partial b_{22}}{\partial x_n} + a_{33}\frac{\partial b_{33}}{\partial x_n} + 2a_{23}\frac{\partial b_{23}}{\partial x_n}), \\ &Num_2 = 2i\frac{\omega}{c}\frac{\partial A_{44}}{\partial x_n}(a_{12}\cos\theta + a_{13}\sin\theta) + \frac{\partial A_{44}}{\partial x_n}(a_{22} + a_{33}), \\ &Den = \frac{\omega}{c^2}(-a_{11}A_{44} + a_{22}b_{22} + a_{33}b_{33} + 2a_{23}b_{23}) \\ &\quad + a_{12}i\cos\theta\frac{A_{44}}{c} + a_{13}i\sin\theta\frac{A_{44}}{c}, \end{aligned} \tag{43}$$

where $a_{ij}, i, j = 1, 2, 3$, represents the leading principal minors of the **G** matrix defined in Eq. (16). Expanding Eq. (43) in terms of stiffness D and A_{44} yields:

$$\begin{aligned} &\frac{\partial c}{\partial D_{11}} = \frac{\omega}{2c}\frac{a_{22}\cos^2\theta}{Den}, \\ &\frac{\partial c}{\partial D_{22}} = \frac{\omega}{2c}\frac{a_{33}\sin^2\theta}{Den}, \\ &\frac{\partial c}{\partial D_{66}} = \frac{\omega}{2c}\frac{a_{22}\sin^2\theta + a_{33}\cos^2\theta + 2a_{23}\sin\theta\cos\theta}{Den}, \\ &\frac{\partial c}{\partial D_{12}} = \frac{\omega}{c}\frac{a_{23}\sin\theta\cos\theta}{Den}, \\ &\frac{\partial c}{\partial D_{16}} = \frac{\omega}{c}\frac{a_{22}\sin\theta\cos\theta + a_{23}\cos^2\theta}{Den}, \\ &\frac{\partial c}{\partial D_{26}} = \frac{\omega}{c}\frac{a_{33}\sin\theta\cos\theta + a_{23}\sin^2\theta}{Den}, \\ &\frac{\partial c}{\partial A_{44}} = \frac{c}{2\omega}\frac{-\frac{\omega^2}{c^2}a_{11} + 2i\frac{\omega}{c}(a_{12}\cos\theta + a_{13}\sin\theta) + (a_{22} + a_{33})}{Den}. \end{aligned} \tag{44}$$

Appendix D. The partial derivative of objective residual with respect to impact location

To solve the optimisation problem for impact localisation illustrated in Eq. (32) using the trust-region-reflective algorithm, the first and

second-order derivatives $\frac{\partial R}{\partial x}$, $\frac{\partial R}{\partial y}$, $\frac{\partial^2 R}{\partial x^2}$, $\frac{\partial^2 R}{\partial y^2}$, and $\frac{\partial^2 R}{\partial x \partial y}$ of objective residual R defined in Eq. (32) with respect to impact location coordinates x and y are required. These derivatives are derived using the chain rule:

$$\begin{aligned}
&\frac{\partial R}{\partial x} = \sum_{j=2}^{N_s} 2r\frac{\partial r}{\partial x}, \quad \frac{\partial R}{\partial y} = \sum_{j=2}^{N_s} 2r\frac{\partial r}{\partial y},\\
&\frac{\partial^2 R}{\partial x^2} = \sum_{j=2}^{N_s} 2(\frac{\partial r}{\partial x})^2 + 2r\frac{\partial^2 r}{\partial x^2},\\
&\frac{\partial^2 R}{\partial y^2} = \sum_{j=2}^{N_s} 2(\frac{\partial r}{\partial y})^2 + 2r\frac{\partial^2 r}{\partial y^2},\\
&\frac{\partial^2 R}{\partial x \partial y} = \sum_{j=2}^{N_s} 2\frac{\partial r}{\partial x}\frac{\partial r}{\partial y} + 2r\frac{\partial^2 r}{\partial x \partial y}.
\end{aligned} \tag{45}$$

These intermediate derivatives $\frac{\partial r}{\partial x}$, $\frac{\partial r}{\partial y}$, $\frac{\partial^2 r}{\partial x^2}$, $\frac{\partial^2 r}{\partial y^2}$, and $\frac{\partial^2 r}{\partial x \partial y}$, are further derived as follows:

$$\begin{aligned}
&\frac{\partial r}{\partial x} = \frac{\partial t_j}{\partial x} - \frac{\partial t_1}{\partial x}, \quad \frac{\partial t_j}{\partial x} = (\frac{1}{c(\theta_j)}\frac{\partial d_j}{\partial x} - \frac{d_j}{c^2(\theta_j)}\frac{\partial c(\theta_j)}{\partial x}),\\
&\frac{\partial r}{\partial y} = \frac{\partial t_j}{\partial y} - \frac{\partial t_1}{\partial y}, \quad \frac{\partial t_j}{\partial y} = (\frac{1}{c(\theta_j)}\frac{\partial d_j}{\partial y} - \frac{d_j}{c^2(\theta_j)}\frac{\partial c(\theta_j)}{\partial y}),\\
&\frac{\partial^2 r}{\partial x^2} = \frac{\partial^2 t_j}{\partial x^2} - \frac{\partial^2 t_1}{\partial x^2},\\
&\frac{\partial^2 t_j}{\partial x^2} = (\frac{1}{c(\theta_j)}\frac{\partial^2 d_j}{\partial x^2} - \frac{1}{c^2(\theta_j)}\frac{\partial c(\theta_j)}{\partial x}\frac{\partial d_j}{\partial x})\\
&\qquad -[(\frac{1}{c^2(\theta_j)}\frac{\partial d_j}{\partial x} + \frac{-2d_j}{c^3(\theta_j)}\frac{\partial c(\theta_j)}{\partial x})\frac{\partial c(\theta_j)}{\partial x} + \frac{d_j}{c^2(\theta_j)}\frac{\partial^2 c(\theta_j)}{\partial x^2}],\\
&\frac{\partial^2 r}{\partial y^2} = \frac{\partial^2 t_j}{\partial y^2} - \frac{\partial^2 t_1}{\partial y^2},\\
&\frac{\partial^2 t_j}{\partial y^2} = (\frac{1}{c(\theta_j)}\frac{\partial^2 d_j}{\partial y^2} - \frac{1}{c^2(\theta_j)}\frac{\partial c(\theta_j)}{\partial y}\frac{\partial d_j}{\partial y})\\
&\qquad -[(\frac{1}{c^2(\theta_j)}\frac{\partial d_j}{\partial y} + \frac{-2d_j}{c^3(\theta_j)}\frac{\partial c(\theta_j)}{\partial y})\frac{\partial c(\theta_j)}{\partial y} + \frac{d_j}{c^2(\theta_j)}\frac{\partial^2 c(\theta_j)}{\partial y^2}],\\
&\frac{\partial^2 r}{\partial x \partial y} = \frac{\partial^2 t_j}{\partial x \partial y} - \frac{\partial^2 t_1}{\partial x \partial y},\\
&\frac{\partial^2 t_j}{\partial x \partial y} = (\frac{1}{c(\theta_j)}\frac{\partial^2 d_j}{\partial x \partial y} - \frac{1}{c^2(\theta_j)}\frac{\partial c(\theta_j)}{\partial y}\frac{\partial d_j}{\partial x})\\
&\qquad -[(\frac{1}{c^2(\theta_j)}\frac{\partial d_j}{\partial y} + \frac{-2d_j}{c^3(\theta_j)}\frac{\partial c(\theta_j)}{\partial y})\frac{\partial c(\theta_j)}{\partial x} + \frac{d_j}{c^2(\theta_j)}\frac{\partial^2 c(\theta_j)}{\partial x \partial y}],\\
&\frac{\partial d_j}{\partial x} = \frac{x - x_j}{d_j}, \quad \frac{\partial d_j}{\partial y} = \frac{y - y_j}{d_j},\\
&\frac{\partial^2 d_j}{\partial x^2} = \frac{(y-y_j)^2}{d_j^3}, \quad \frac{\partial^2 d_j}{\partial y^2} = \frac{(x-x_j)^2}{d_j^3}, \quad \frac{\partial^2 d_j}{\partial x \partial y} = \frac{-(x-x_j)(y-y_j)}{d_j^3}.
\end{aligned} \tag{46}$$

Since the optimised WVP maintains a fixed shape and value, the intermediate derivatives, $\frac{\partial c(\theta_j)}{\partial x}$, $\frac{\partial c(\theta_j)}{\partial y}$, $\frac{\partial^2 c(\theta_j)}{\partial x^2}$, $\frac{\partial^2 c(\theta_j)}{\partial y^2}$, $\frac{\partial^2 c(\theta_j)}{\partial x \partial y}$ are non-zero only when the optimised WVP exhibits non-circular wavefronts. This is because even small variations in the location coordinates x, y result in changes in the wave propagation direction θ, thereby altering the wave propagation velocity $c(\theta)$. These derivatives can be derived using the chain rule:

$$\begin{aligned}
&\frac{\partial c(\theta_j)}{\partial x} = \frac{\partial c(\theta_j)}{\partial \theta_j}\frac{\partial \theta_j}{\partial x}, \quad \frac{\partial c(\theta_j)}{\partial y} = \frac{\partial c(\theta_j)}{\partial \theta_j}\frac{\partial \theta_j}{\partial y},\\
&\frac{\partial^2 c(\theta_j)}{\partial x^2} = \frac{\partial^2 c(\theta_j)}{\partial \theta_j^2}(\frac{\partial \theta_j}{\partial x})^2 + \frac{\partial c(\theta_j)}{\partial \theta_j}\frac{\partial^2 \theta_j}{\partial x^2},\\
&\frac{\partial^2 c(\theta_j)}{\partial y^2} = \frac{\partial^2 c(\theta_j)}{\partial \theta_j^2}(\frac{\partial \theta_j}{\partial y})^2 + \frac{\partial c(\theta_j)}{\partial \theta_j}\frac{\partial^2 \theta_j}{\partial y^2},\\
&\frac{\partial^2 c(\theta_j)}{\partial x \partial y} = \frac{\partial^2 c(\theta_j)}{\partial \theta_j^2}\frac{\partial \theta_j}{\partial x}\frac{\partial \theta_j}{\partial y} + \frac{\partial c(\theta_j)}{\partial \theta_j}\frac{\partial^2 \theta_j}{\partial x \partial y}.
\end{aligned} \tag{47}$$

The computation of these intermediate derivatives involves the derivatives of the WVP $c(\theta)$ with respect to the direction θ and the derivatives of the direction θ with respect to the impact coordinates (x, y). As the wave propagation direction θ_j is given by $\cos(\theta_j) = (x_j - x)/d_j$, the partial derivatives of θ_j with respect to impact location (x, y) are derived as:

$$\begin{aligned}
&\frac{\partial \theta_j}{\partial x} = \frac{(y_j - y)}{(x_j - x)^2 + (y_j - y)^2} = \frac{(y_j - y)}{d_j^2},\\
&\frac{\partial \theta_j}{\partial y} = \frac{-(x_j - x)}{(x_j - x)^2 + (y_j - y)^2} = \frac{(x - x_j)}{d_j^2},\\
&\frac{\partial^2 \theta_j}{\partial x^2} = \frac{2(x - x_j)(y - y_j)}{d_j^4}, \quad \frac{\partial^2 \theta_j}{\partial y^2} = \frac{-2(x - x_j)(y - y_j)}{d_j^4},\\
&\frac{\partial^2 \theta_j}{\partial x \partial y} = \frac{(y - y_j)^2 - (x - x_j)^2}{d_j^4}.
\end{aligned} \tag{48}$$

Based on the first and second-order derivatives of the dispersion equation shown in Eqs. (18) and (19), the first and second-order derivatives of $g_{ij}, i, j = 1, 2, 3$, with respect to the direction θ are required for the calculation of $\frac{\partial c(\theta)}{\partial \theta}$, $\frac{\partial^2 c(\theta)}{\partial \theta^2}$, which can be derived as:

$$\begin{aligned}
&\frac{\partial g_{11}}{\partial \theta} = 2A_{44}\frac{\omega^2}{c^3}\frac{\partial c}{\partial \theta}, \quad \frac{\partial^2 g_{11}}{\partial \theta^2} = 2A_{44}\omega^2(\frac{1}{c^3}\frac{\partial^2 c}{\partial \theta^2} - 3\frac{1}{c^4}(\frac{\partial c}{\partial \theta})^2),\\
&\frac{\partial g_{12}}{\partial \theta} = -iA_{44}\omega(\frac{\cos\theta}{c^2}\frac{\partial c}{\partial \theta} + \frac{\sin\theta}{c}),\\
&\frac{\partial^2 g_{12}}{\partial \theta^2} = -iA_{44}\omega[-2\frac{\sin\theta}{c^2}\frac{\partial c}{\partial \theta} - 2\frac{\cos\theta}{c^3}(\frac{\partial c}{\partial \theta})^2 + \frac{\cos\theta}{c^2}\frac{\partial^2 c}{\partial \theta^2} + \frac{\cos\theta}{c}],\\
&\frac{\partial g_{13}}{\partial \theta} = iA_{44}\omega(-\frac{\sin\theta}{c^2}\frac{\partial c}{\partial \theta} + \frac{\cos\theta}{c}),\\
&\frac{\partial^2 g_{13}}{\partial \theta^2} = iA_{44}\omega[-2\frac{\cos\theta}{c^2}\frac{\partial c}{\partial \theta} + 2\frac{\sin\theta}{c^3}(\frac{\partial c}{\partial \theta})^2 - \frac{\sin\theta}{c^2}\frac{\partial^2 c}{\partial \theta^2} - \frac{\sin\theta}{c}],\\
&\frac{\partial g_{22}}{\partial \theta} = -2b_{22}\frac{\omega^2}{c^3}\frac{\partial c}{\partial \theta} + b'_{22}\frac{\omega^2}{c^2},\\
&\frac{\partial^2 g_{22}}{\partial \theta^2} = b''_{22}\frac{\omega^2}{c^2} - 4b'_{22}\frac{\omega^2}{c^3}\frac{\partial c}{\partial \theta} - 2\omega^2 b_{22}(-3\frac{1}{c^4}(\frac{\partial c}{\partial \theta})^2 + \frac{1}{c^3}\frac{\partial^2 c}{\partial \theta^2}),\\
&\frac{\partial g_{23}}{\partial \theta} = -2b_{23}\frac{\omega^2}{c^3}\frac{\partial c}{\partial \theta} + b'_{23}\frac{\omega^2}{c^2},\\
&\frac{\partial^2 g_{23}}{\partial \theta^2} = b''_{23}\frac{\omega^2}{c^2} - 4b'_{23}\frac{\omega^2}{c^3}\frac{\partial c}{\partial \theta} - 2\omega^2 b_{23}(-3\frac{1}{c^4}(\frac{\partial c}{\partial \theta})^2 + \frac{1}{c^3}\frac{\partial^2 c}{\partial \theta^2}),\\
&\frac{\partial g_{33}}{\partial \theta} = -2b_{33}\frac{\omega^2}{c^3}\frac{\partial c}{\partial \theta} + b'_{33}\frac{\omega^2}{c^2},\\
&\frac{\partial^2 g_{33}}{\partial \theta^2} = b''_{33}\frac{\omega^2}{c^2} - 4b'_{33}\frac{\omega^2}{c^3}\frac{\partial c}{\partial \theta} - 2\omega^2 b_{33}(-3\frac{1}{c^4}(\frac{\partial c}{\partial \theta})^2 + \frac{1}{c^3}\frac{\partial^2 c}{\partial \theta^2}),
\end{aligned} \tag{49}$$

where b_{ij} is a component of g_{ij} as defined in Eq. (10), b'_{ij} and b''_{ij} represent the first and second partial derivatives of b_{ij} with respect to direction θ, respectively, and they are given by:

$$\begin{aligned}
&b'_{22} = (D_{66} - D_{11})\sin 2\theta + 2D_{16}\cos 2\theta,\\
&b''_{22} = 2(D_{66} - D_{11})\cos 2\theta - 4D_{16}\sin 2\theta,\\
&b'_{23} = (D_{26} - D_{16})\sin 2\theta + (D_{12} + D_{66})\cos 2\theta,\\
&b''_{23} = 2(D_{26} - D_{16})\cos 2\theta - 2(D_{12} + D_{66})\sin 2\theta,\\
&b'_{33} = (D_{22} - D_{66})\sin 2\theta + 2D_{26}\cos 2\theta,\\
&b''_{33} = 2(D_{22} - D_{66})\cos 2\theta - 4D_{26}\sin 2\theta.
\end{aligned} \tag{50}$$

Combining Eqs. (49) and (50) with Eq. (18), the first-order derivative of velocity $c(\theta)$ with respect to direction θ ($\frac{\partial c(\theta)}{\partial \theta}$) is given by:

$$\frac{\partial c(\theta)}{\partial \theta} = \frac{\frac{\omega}{c}(a_{22}b'_{22} + a_{33}b'_{33} + 2a_{23}b'_{23}) + 2iA_{44}(a_{13}\cos\theta - a_{12}\sin\theta)}{2\frac{\omega}{c^2}(a_{22}b_{22} + a_{33}b_{33} + 2a_{23}b_{23} - a_{11}A_{44}) + \frac{2iA_{44}}{c}(a_{12}\cos\theta + a_{13}\sin\theta)}. \tag{51}$$

Representing $\frac{\partial^2 g_{ij}}{\partial \theta^2} = e_{ij} - q_{ij}\frac{\partial^2 c}{\partial \theta^2}, i, j = 1, 2, 3$, as shown in Eq. (49), where $e_{ij}, i, j = 1, 2, 3$, does not include terms related to $\frac{\partial^2 c}{\partial \theta^2}$, the second-order derivative of the velocity $c(\theta)$ with respect to the direction ($\frac{\partial^2 c(\theta)}{\partial \theta^2}$) can be derived by substituting Eqs. (49)–(51) into Eq. (19):

$$\frac{\partial^2 c(\theta)}{\partial \theta^2} = \frac{\sum_{i=1}^{3}\sum_{j=1}^{3}\frac{\partial a_{ij}}{\partial \theta}\frac{\partial g_{ij}}{\partial \theta} + \sum_{i=1}^{3}\sum_{j=1}^{3} a_{ij}e_{ij}}{\sum_{i=1}^{3}\sum_{j=1}^{3} a_{ij}q_{ij}}. \tag{52}$$

References

[1] Zou J, Lei Z, Bai R, Liu D, Jiang H, Liu J, et al. Damage and failure analysis of composite stiffened panels under low-velocity impact and compression after impact. Compos Struct 2021;262:113333.

[2] Thorsson SI, Sringeri SP, Waas AM, Justusson BP, Rassaian M. Experimental investigation of composite laminates subject to low-velocity edge-on impact and compression after impact. Compos Struct 2018;186:335–46.

[3] Hassoon OH, Tarfaoui M, El Malki Alaoui A, El Moumen A. Mechanical behavior of composite structures subjected to constant slamming impact velocity: An experimental and numerical investigation. Int J Mech Sci 2018;144:618–27.

[4] Jribi K, Gosse JH, Neill DJ, Mello AW. Damage control measures in composites: BVID damage progression. American Society of Mechanical Engineers Digital Collection; 2023, http://dx.doi.org/10.1115/SSDM2023-100771.

[5] Bouvet C, Rivallant S. 2 - Damage tolerance of composite structures under low-velocity impact. In: Silberschmidt V, editor. Dynamic deformation, damage and fracture in composite materials and structures (second edition). Woodhead publishing series in composites science and engineering, Woodhead Publishing; 2023, p. 3–28. http://dx.doi.org/10.1016/B978-0-12-823979-7.00002-8.

[6] Sause MGR, Jasiūnienė E, editors. Structural health monitoring damage detection systems for aerospace. Springer Nature; 2021, http://dx.doi.org/10.1007/978-3-030-72192-3.

[7] Fu H, Sharif Khodaei Z, Aliabadi MHF. An event-triggered energy-efficient wireless structural health monitoring system for impact detection in composite airframes. IEEE Internet Things J 2019;6:1183–92.

[8] Beligni A, Kowalczyk K, Sbarufatti C, Giglio M. An impact monitoring system for aeronautical structures. In: Rizzo P, Milazzo A, editors. European workshop on structural health monitoring. Lecture notes in civil engineering, Cham: Springer International Publishing; 2021, p. 636–46. http://dx.doi.org/10.1007/978-3-030-64594-6_62.

[9] Aliabadi MHF, Sharif Khodaei Z. Structural health monitoring for advanced composite structures. In: Computational and experimental methods in structures, vol. 08, EUROPE: WORLD SCIENTIFIC; 2018, http://dx.doi.org/10.1142/q0114.

[10] Farrar CR, Worden K. Structural health monitoring: A machine learning perspective. Chichester, West Sussex, U.K.; Hoboken, N.J: Wiley; 2013.

[11] Giannaros E, Kotzakolios A, Kostopoulos V, Sotiriadis G, Vignjevic R, Djordjevic N, et al. Low- and high-fidelity modeling of sandwich-structured composite response to bird strike, as tools for a digital-twin-assisted damage diagnosis. Int J Impact Eng 2022;160:104058.

[12] Zaparoli Cunha B, Droz C, Zine A-M, Foulard S, Ichchou M. A review of machine learning methods applied to structural dynamics and vibroacoustic. Mech Syst Signal Process 2023;200:110535.

[13] Hu N, Fukunaga H, Matsumoto S, Yan B, Peng XH. An efficient approach for identifying impact force using embedded piezoelectric sensors. Int J Impact Eng 2007;34:1258–71.

[14] El-Bakari A, Khamlichi A, Jacquelin E, Dkiouak R. Assessing impact force localization by using a particle swarm optimization algorithm. J Sound Vib 2014;333:1554–61.

[15] Liu Y, Wang L. Quantification, localization, and reconstruction of impact force on interval composite structures. Int J Mech Sci 2023;239:107873.

[16] Giammaria V, Del Bianco G, Raponi E, Fiumarella D, Ciardiello R, Boria S, et al. Material parameter optimization of flax/epoxy composite laminates under low-velocity impact. Compos Struct 2023;321:117303.

[17] Xu T, Wang Z, Hu Y, Du S, Du A, Yu Z, et al. A FEM-based direct method for identification of Young's modulus and boundary conditions in three-dimensional linear elasticity from local observation. Int J Mech Sci 2023;237:107797.

[18] Xiao D, Khodaei ZS, Aliabadi MHF. Impact Identification Based on Surrogate-assisted Efficient Global Optimisation. Procedia Struct Integr 2024;52:667–78.

[19] Geradin M, Rixen DJ. Mechanical vibrations: Theory and application to structural dynamics. John Wiley & Sons; 2014.

[20] Goutaudier D, Gendre D, Kehr-Candille V, Ohayon R. Impulse identification technique by estimating specific modal ponderations from vibration measurements. J Sound Vib 2020;474:115263.

[21] Goutaudier D, Gendre D, Kehr-Candille V, Ohayon R. Single-sensor approach for impact localization and force reconstruction by using discriminating vibration modes. Mech Syst Signal Process 2020;138:106534.

[22] Fink M. Time reversal of ultrasonic fields. I. Basic principles. IEEE Trans Ultrason Ferroelectr Freq Control 1992;39:555–66, Conference Name: IEEE Transactions on Ultrasonics, Ferroelectrics, and Frequency Control.

[23] Ciampa F, Meo M. Impact detection in anisotropic materials using a time reversal approach. Struct Health Monit 2012;11:43–9.

[24] Yu Z, Xu C, Sun J, Du F. Impact localization and force reconstruction for composite plates based on virtual time reversal processing with time-domain spectral finite element method. Struct Health Monit 2023;22:4149–70.

[25] Simone MED, Ciampa F, Meo M. A hierarchical method for the impact force reconstruction in composite structures. Smart Mater Struct 2019;28:085022.

[26] Chen C, Li Y, Yuan F-G. Impact source identification in finite isotropic plates using a time-reversal method: Experimental study. Smart Mater Struct 2012;21:105025.

[27] Park B, Sohn H, Olson SE, DeSimio MP, Brown KS, Derriso MM. Impact localization in complex structures using laser-based time reversal. Struct Health Monit 2012;11:577–88.

[28] Kundu T. Acoustic source localization. Ultrasonics 2014;54:25–38.

[29] Moon FC. A critical survey of wave propagation and impact in composite materials. Technical Report NASA-CR-121226, 1973.

[30] Daniel IM, Liber T, LaBedz RH. Wave propagation in transversely impacted composite laminates. Exp Mech 1979;19:9.

[31] Tan TM, Sun CT. Wave propagation in graphite/epoxy laminates due to impact. Technical Report NASA-CR-168057, 1982.

[32] Capineri L, Bulletti A. A versatile analog electronic interface for piezoelectric sensors used for impacts detection and positioning in structural health monitoring (SHM) systems. Electronics 2021;10:1047.

[33] Bulletti A, Merlo EM, Capineri L. Analysis of the accuracy in impact localization using piezoelectric sensors for Structural Health Monitoring with multichannel real-time electronics. In: 2020 IEEE 7th international workshop on metrology for aeroSpace. 2020, p. 480–4. http://dx.doi.org/10.1109/MetroAeroSpace48742.2020.9160275.

[34] Zhu K, Qing XP, Liu B, He T. A passive localization method for stiffened composite structures with a parameterized laminate model. J Sound Vib 2020;489:115683.

[35] Meo M, Zumpano G, Piggott M, Marengo G. Impact identification on a sandwich plate from wave propagation responses. Compos Struct 2005;71:302–6.

[36] Sikdar S, Mirgal P, Banerjee S. Low-velocity impact source localization in a composite sandwich structure using a broadband piezoelectric sensor network. Compos Struct 2022;291:115619.

[37] Coverley PT, Staszewski WJ. Impact damage location in composite structures using optimized sensor triangulation procedure. Smart Mater Struct 2003;12:795.

[38] Jang B-W, Kim C-G. Impact localization of composite stiffened panel with triangulation method using normalized magnitudes of fiber optic sensor signals. Compos Struct 2019;211:522–9.

[39] Cuomo S, Bätzel T, Modler N, Hornig A, Meo M. High velocity impact on generic CFRP blade specimen: Baseline free method for impact localisation and damage assessment on complex structures. Smart Mater Struct 2022;31:065024.

[40] Jones MR, Rogers TJ, Worden K, Cross EJ. A Bayesian methodology for localising acoustic emission sources in complex structures. Mech Syst Signal Process 2022;163:108143.

[41] Balasubramanian P, Kaushik V, Altamimi SY, Amabili M, Alteneiji M. Comparison of neural networks based on accuracy and robustness in identifying impact location for structural health monitoring applications. Struct Health Monit 2023;22:417–32.

[42] Dipietrangelo F, Nicassio F, Scarselli G. Impact characterization on thin structures using machine learning approaches. Chin J Aeronaut 2024;37:30–44.

[43] Huan S, Lu L, Shen T, Du J. Low velocity impact monitoring of composite tubes based on FBG sensors. Sensors 2024;24:1279, Number: 4 Publisher: Multidisciplinary Digital Publishing Institute.

[44] Dipietrangelo F, Nicassio F, Scarselli G. Structural Health Monitoring for impact localisation via machine learning. Mech Syst Signal Process 2023;183:109621.

[45] Morse L, Sharif Khodaei Z, Aliabadi MH. Reliability based impact localization in composite panels using Bayesian updating and the Kalman filter. Mech Syst Signal Process 2018;99:107–28.

[46] Dehghan Niri E, Farhidzadeh A, Salamone S. Nonlinear Kalman Filtering for acoustic emission source localization in anisotropic panels. Ultrasonics 2014;54:486–501.

[47] Sharif-Khodaei Z, Ghajari M, Aliabadi MH. Determination of impact location on composite stiffened panels. Smart Mater Struct 2012;21:105026.

[48] Seno AH, Sharif Khodaei Z, Aliabadi MHF. Passive sensing method for impact localisation in composite plates under simulated environmental and operational conditions. Mech Syst Signal Process 2019;129:20–36.

[49] Seno AH, Aliabadi MHF. Impact localisation in composite plates of different stiffness impactors under simulated environmental and operational conditions. Sensors 2019;19:3659.

[50] Seno AH, Aliabadi MF. Uncertainty quantification for impact location and force estimation in composite structures. Struct Health Monit 2021;147592172110202.

[51] Houdek V, Smolík L, Kubín Z. Impact point localization in three-dimensional structures using wavelet transform. Mech Syst Signal Process 2022;179:109365.

[52] Qiu B, Zhang M, Li X, Qu X, Tong F. Unknown impact force localisation and reconstruction in experimental plate structure using time-series analysis and pattern recognition. Int J Mech Sci 2020;166:105231.

[53] Liu Q, Wang F, Li J, Xiao W. A hybrid support vector regression with multi-domain features for low-velocity impact localization on composite plate structure. Mech Syst Signal Process 2021;154:107547.

[54] Liu Q, Wang F, Liu M, Xiao W. A two-step localization method using wavelet packet energy characteristics for low-velocity impacts on composite plate structures. Mech Syst Signal Process 2023;188:110061.

[55] Damm AM, Spitzmüller C, Raichle ATS, Bühler A, Weißgraeber P, Middendorf P. Deep learning for impact detection in composite plates with sparsely integrated sensors. Smart Mater Struct 2020;29:125014.

[56] Zhao B, Wang Y, Zeng X, Qing X. Impact monitoring on complex structure using VMD-MPE feature extraction and transfer learning. Ultrasonics 2024;136:107141.

[57] Zargar SA, Yuan F-G. Impact diagnosis in stiffened structural panels using a deep learning approach. Struct Health Monit 2021;20:681–91.

[58] Aucejo M. A data-driven metamodel-based approach for point force localization. Mech Syst Signal Process 2022;171:108881.

[59] Miele S, Karve P, Mahadevan S. Multi-fidelity physics-informed machine learning for probabilistic damage diagnosis. Reliab Eng Syst Saf 2023;235:109243.

[60] Torzoni M, Manzoni A, Mariani S. A multi-fidelity surrogate model for structural health monitoring exploiting model order reduction and artificial neural networks. Mech Syst Signal Process 2023;197:110376.

[61] Makkar G, Smith C, Drakoulas G, Kopsaftopoulos F, Gandhi F. A machine learning framework for physics-based multi-fidelity modeling and health monitoring for a composite wing. In: Volume 1: acoustics, vibration, and phononics. 2022.

[62] Hami Seno A, Ferri Aliabadi MH. Multifidelity data augmentation for data driven passive impact location and force estimation in composite structures under simulated environmental and operational conditions. Mech Syst Signal Process 2023;195:110288.

[63] Kalimullah NMM, Shelke A, Habib A. A probabilistic framework for source localization in anisotropic composite using transfer learning based multi-fidelity physics informed neural network (mfPINN). Mech Syst Signal Process 2023;197:110360.

[64] Timoshenko S, Woinowsky-Krieger S. Theory of Plates and Shells. McGraw-Hill; 1959.

[65] Coleman TF, Li Y. An interior trust region approach for nonlinear minimization subject to bounds. SIAM J Optim 1996;6:418–45.

[66] Jones RM. Mechanics of composite materials. Washington DC: McGraw-Hill; 1975.

[67] Tsai S. Introduction to composite materials. Lancaster, Pennsylvania: Technomic Publishing Co; 1980, http://dx.doi.org/10.1201/9780203750148.
[68] Forrester AIJ, Sbester A, Keane AJ. Engineering design via surrogate modelling. Chichester, UK: John Wiley & Sons, Ltd; 2008, http://dx.doi.org/10.1002/9780470770801.
[69] Kalman RE. A new approach to linear filtering and prediction problems. J Basic Eng 1960;82:35–45.
[70] Correas AC, Crespo AC, Ghasemnejad H, Roshan G. Analytical solutions to predict impact behaviour of stringer stiffened composite aircraft panels. Appl Compos Mater 2021;28:1237–54.
[71] Mallardo V, Sharif Khodaei Z, Aliabadi FMH. A Bayesian approach for sensor optimisation in impact identification. Materials 2016;9:946.
[72] Ostachowicz W, Soman R, Malinowski P. Optimization of sensor placement for structural health monitoring: A review. Struct Health Monit 2019;18:963–88.
[73] Khodaei S. An optimization strategy for best sensor placement for damage detection and localization in complex composite structures. In: 8th European workshop on structural health monitoring. 2016.
[74] Abrate S. Impact on composite structures. Cambridge: Cambridge University Press; 1998, http://dx.doi.org/10.1017/CBO9780511574504.
[75] Tang BS. Lamb wave propagation in laminated composite plates. Virginia Polytechnic Institute and State University; 1988, accepted: 2017-11-09T21:16:32Z.
[76] Seydel R, Chang F-K. Impact identification of stiffened composite panels: I. System development. Smart Mater Struct 2001;10:354–69.